Article

Origins of Superstructure Ordering and Incommensurability in Stuffed CoSn-Type Phases

Daniel C. Fredrickson, Sven Lidin, Gerard Venturini, Bernard Malaman, and Jeppe Christensen

More About This Article

Additional resources and features associated with this article are available within the HTML version:

- Supporting Information
- Links to the 1 articles that cite this article, as of the time of this article download
- Access to high resolution figures
- Links to articles and content related to this article
- Copyright permission to reproduce figures and/or text from this article

View the Full Text HTML

Origins of Superstructure Ordering and Incommensurability in Stuffed CoSn-Type Phases

Daniel C. Fredrickson,*,† Sven Lidin,† Gerard Venturini,‡ Bernard Malaman,‡ and Jeppe Christensen†

Inorganic Chemistry, Arrhenius Laboratory, Stockholm University, 106 91 Stockholm, Sweden, and Laboratoire de Chimie du Solide Minéral, Université Henri Poincaré-Nancy I, associé au CNRS (UMR 7555), B.P. 239, 54506 Vandoeuvre les Nancy Cedex, France

Received September 26, 2007; E-mail: danny@inorg.su.se

Abstract: The CoSn structure type contains large interstitial void spaces that frequently host electropositive guest atoms, such as rare earth elements. In this stuffing process, an intriguing ordering occurs between the neighboring void spaces leading to a family of long-period superstructures comprising intergrowths of the $ScFe_6Ge_6$ and $ScFe_6Ga_6$ structure types. This superstructure ordering culminates in incommensurability in the $REFe_6Ge_{6-\delta}Ga_\delta$ systems with RE = Sc, Tb, and Lu. In this work, we derive a 3 + 1D superspace model encompassing this series of structures and investigate the origins of the structural trends in this family with electronic structure calculations, at both the LDA-DFT and extended Hückel levels. Using our 3 + 1D model, we refine the structures of four new $ErFe_6Ge_{6-\delta}Ga_\delta$ ($0 \leq \delta \leq 6$) phases, two commensurate and two incommensurate, from powder X-ray diffraction data. The refinement results confirm trends observed in the Sc-, Tb-, and Lu-based series: a gradual lengthening and, eventually, turning of the q-vector as Ge is progressively exchanged for Ga. These trends, and the incommensurate ordering as a whole, are traced to a tension between two modes by which the host lattice responds to stuffing atom insertion: (1) an atomic charge modulation enhancing the anionic character of the cavity walls around the guest atoms, and (2) a positional modulation expanding the cavities occupied by guest atoms. These two modes direct the stuffing atom ordering pattern toward opposite ends of the $ScFe_6Ge_6$–$ScFe_6Ga_6$ intergrowth series. The full series of structures, complex and incommensurate, reflects various degrees of balance between these two factors.

1. Introduction

Stuffing extra atoms into the void spaces of a parent structure is a common motif in solid state chemistry. Examples in the intermetallics field alone include the clathrates,[1–5] filled skutterudites,[6–8] and stuffed derivatives of the Mn_5Si_3- and $BaHg_{11}$-types.[9–13] When the filling of these void spaces is only partial, the possibility of ordered patterns of guest atom inclusion arises. So far, superstructures of the host-lattice arising from stuffing patterns have been observed only sparingly,[9,10,14,15] but the effects of such ordering in X-ray diffraction measurements can be quite weak and could be easily missed, particularly in the era before area detectors. There are some families of stuffed compounds, however, where guest atom ordering forms the basis of an extensive structural chemistry. Vivid instances of this are transition metal interstitial carbides,[16–18] filled NiAs-type phases,[19] and stuffed versions of the CoSn structure type.[20] In all of these systems, long-period or even incommensurate structures arise, all based on the simplest of packing principles: inserting atoms into the empty spaces of a host structure. Evidently some form of communication between stuffing atoms directs the formation of these occupation patterns. In this paper, we will team superspace analysis with electronic structure calculations to decode this communication in one of these families, the stuffed variants of the CoSn-type (Figure 1).
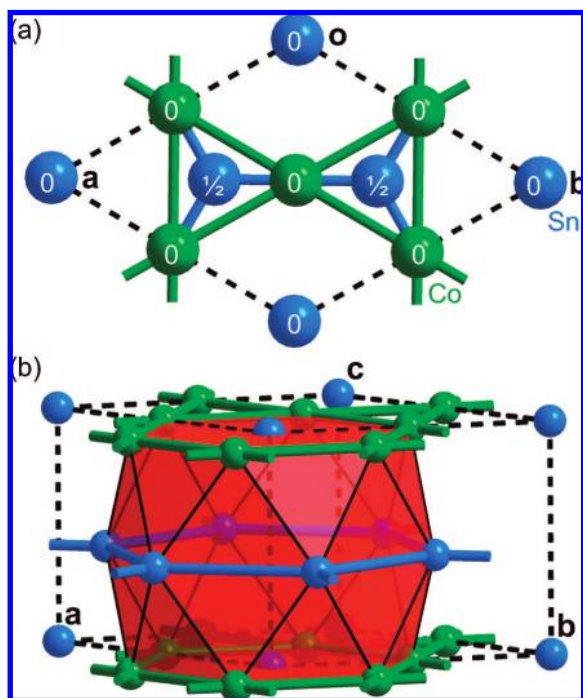
In the CoSn-type, an alternation of Sn-centered Co kagomé nets (green) with Sn honeycomb nets (blue) creates large hexagonal void spaces (red polyhedron in Figure 1b), which

† Stockholm University.
‡ Université Henri Poincaré-Nancy I.

(1) Kasper, J. S.; Hagenmuller, P.; Pouchard, M.; Cros, C. *Science* **1965**, *150*, 1713–1714.
(2) Bobev, S.; Sevov, S. C. *J. Am. Chem. Soc.* **1999**, *121*, 3795–3796.
(3) Gryko, J.; McMillan, P. F.; Marzke, R. F.; Ramachandran, G. K.; Patton, D.; Deb, S. K.; Sankey, O. F. *Phys. Rev. B* **2000**, *62*, 7707–7710.
(4) Ammar, A.; Cros, C.; Pouchard, M.; Jaussaud, N.; Bassat, J.-M.; Villeneuve, G.; Duttine, M.; Ménétrier, M.; Reny, E. *Solid State Sci.* **2004**, *6*, 393–400.
(5) Guloy, A. M.; Ramlau, R.; Tang, Z.; Schnelle, W.; Baitinger, M.; Grin, Y. *Nature* **2006**, *443*, 320–323.
(6) Jeitschko, W.; Braun, D. *Acta Crystallogr. B* **1977**, *33*, 3401–3406.
(7) Braun, D. J.; Jeitschko, W. *J. Less-Common Met.* **1980**, *76*, 33–40.
(8) Stetson, N. T.; Kauzlarich, S. M.; Hope, H. *J. Solid State Chem.* **1991**, *91*, 140–147.
(9) Guloy, A. M.; Corbett, J. D. *Inorg. Chem.* **1996**, *35*, 4669–4675.
(10) Larsson, A.-K.; Withers, R. L.; Stenberg, L. *J. Solid State Chem.* **1996**, *127*, 222–230.
(11) Corbett, J. D.; Garcia, E.; Guloy, A. M.; Hurng, W.-M.; Kwon, Y.-U.; Leon-Escamilla, E. A. *Chem. Mater.* **1998**, *10*, 2824–2836.
(12) Latturner, S. E.; Kanatzidis, M. G. *Inorg. Chem.* **2004**, *43*, 2–4.
(13) Li, B.; Corbett, J. D. *Inorg. Chem.* **2006**, *45*, 3861–3863.
(14) Hoffmann, R.-D.; Wachtmann, K. H.; Ebel, T.; Jeitschko, W. *J. Solid State Chem.* **1995**, *118*, 158–162.
(15) Mills, A. M.; Ruck, M. *Inorg. Chem.* **2006**, *45*, 5172–5178.
(16) Yvon, K.; Parthé, E. *Acta. Crystallogr. B* **1970**, *26*, 149–153.
(17) Parthé, E.; Yvon, K. *Acta. Crystallogr. B* **1970**, *26*, 153–163.
(18) Lipatnikov, V. N.; Rempel, A. A. *JEPT Lett.* **2005**, *81*, 326–330.
(19) Lidin, S.; Larsson, A.-K. *J. Solid State Chem.* **1995**, *118*, 313–322.
(20) Venturini, G. *Z. Kristallogr.* **2006**, *221*, 511–520.

Figure 1. The CoSn structure type. (a) View down the *c*-axis. (b) The alternation of Sn-centered Co kagomé nets with Sn honeycomb nets creates hexagonal cavities (red polyhedron), which accommodate guest atoms in stuffed variants of this structure type.

have been deemed "anomalously large".[21] This void space serves host to cationic guest atoms in a series of RET_6E_6 phases (RE = electropositive metallic elements such as the rare earths, Sc and Hf; T = Mn, Fe, Co, Ni; E = Ga, Ge, In, Sn).[20,22–24] These often exhibit intriguing magnetic phenomena such as helimagnetic ordering[25,26] and giant magnetoresistance,[27–30] but most impressive is the wondrous structural variety arising in this family: ordering of the RE atoms creates inclusion patterns (Table 1), with repeat periods ranging from 2 to 68 CoSn subcells.[20,22,31,32] Recently, powder diffraction experiments in the $REFe_6(Ge/Ga)_6$ (RE = Sc, Tb, Lu) systems also revealed structurally incommensurate members of this family.[20,33,34]

(21) Simak, S. I.; Häussermann, U.; Abrikosov, I. A.; Eriksson, O.; Wills, J. M.; Lidin, S.; Johansson, B. *Phys. Rev. Lett.* **1997**, *79*, 1333–1336.
(22) Buchholz, W.; Schuster, H.-U. *Z. Anorg. Allg. Chem.* **1981**, *482*, 40–48.
(23) Olenych, R. R.; Aksel'rud, L. G.; Yarmolyuk, Y. P. *Dopovidi Akademii Nauk Ukrains'koi RSR, Seriya A: Fiziko-Matematichni Ta Tekhnichni Nauki* **1981**, *43*, 87–91.
(24) Belyavina, N. N.; Markiv, V. Y *Dopovidi Akademii Nauk Ukrains'koi RSR, Seriya B: Geologichni, Khimichni ta Biologichni Nauki* **1982**, *12*, 31–34.
(25) Mazet, T.; Welter, R.; Malaman, B. *J. Alloys Comp.* **1999**, *284*, 54–59.
(26) Lefevre, C.; Venturini, G.; Malaman, B. *J. Alloys Comp.* **2002**, *343*, 38–46.
(27) Zhang, S.-Y.; Zhao, P.; Cheng, Z.-H.; Li, R.-W.; Sun, J.-R.; Zhang, H.-W.; Shen, B.-G. *Phys. Rev. B* **2001**, *64*, 212404.1–212404.4.
(28) Canepa, F.; Napoletano, M.; Lefevre, C.; Venturini, G. *J. Alloys Compd.* **2002**, *339*, 26–29.
(29) Yao, J.-L.; Zhang, S.-Y.; Yan, M.; Yang, D.-R.; Wang, R.-W.; Zhang, L.-G.; Shen, B.-G. *J. Appl. Phys.* **2003**, *93*, 10137–10139.
(30) Canepa, F.; Napoletano, M.; Lefevre, C.; Venturini, G. *Physica B* **2003**, *334*, 68–74.
(31) El Idrissi, B. C.; Venturini, G.; Malaman, B. *Mater. Res. Bull.* **1991**, *26*, 1331–1338.
(32) Venturini, G.; Welter, R.; Malaman, B. *J. Alloys Compd.* **1992**, *185*, 99–107.

Table 1. Orthorhombic, Commensurate Intergrowth Structures of the $ScFe_6Ga_6$ and $ScFe_6Ge_6$ Structure Types

structure type	CoSn subcells	n_λ	n_{sc}	space group	ref
$HfFe_6Ge_6$ [a]	2	0	1	*P6/mmm*	23
$ErFe_6Sn_6$	16	1	4	*Amam*	31
$ScFe_6Ge_{2.5}Ga_{3.5}$	44	3	11	*Immm*	33
$HoFe_6Sn_6$	12	1	3	*Immm*	31
YFe_6Sn_6	32	3	8	*Amam*	31
$DyFe_6Sn_6$	20	2	5	*Cmmm*	31
$TbFe_6Sn_6$	8	1	2	*Amam*	31
$TbFe_6Ge_{3.5}Ga_{2.5}$	12	2	3	*Cmmm*	34
$TbFe_6Ge_3Ga_3$	68	12	17	*Cmmm*	34
$ScFe_6Ga_6$	4	1	1	*Immm*	24

[a] We will also frequently refer to this structure as the $ScFe_6Ge_6$ structure type, due its role as one end-member in the progression of structures observed in the $ScFe_6Ge_{6-\delta}Ga_\delta$, $0 \leq \delta \leq 6$ system.
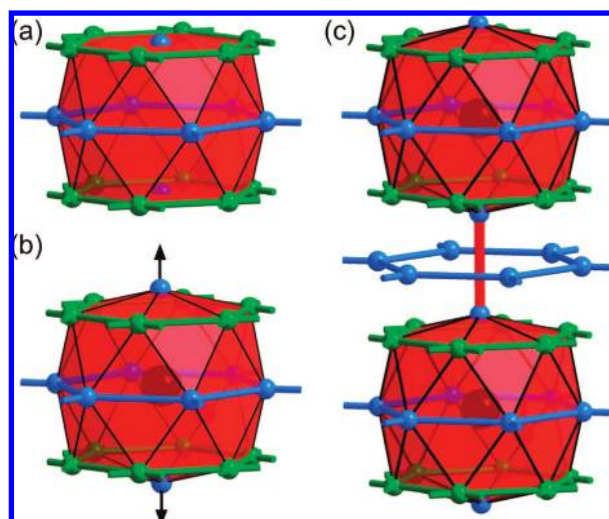

Figure 2. Local rearrangements in the CoSn structure type upon inclusion of stuffing atoms. The hexagonal cavity (a) before and (b) after the incorporation of a guest atom. The insertion of a guest atom forces the capping atoms at top and bottom of the cavity outward. (c) The capping atoms penetrate into the neighboring cavities above and below, rendering the neighboring cavities inaccessible to guest atoms. The filled cavities then alternate with vacant ones, with the capping atoms bumping into each other to form dumbbells across the vacant cavities. Co: green. Sn: blue. Guest atom: large sphere.

The commensurate structures in this family have been examined in some detail, particularly in a recent review by Venturini.[20] A beautiful scheme of cooperativity in guest atom incorporation along the *c*-axis of the CoSn structure type develops (Figure 2): the inclusion of a guest into one of these cavities pushes the Sn sites at the top and bottom of the void space away from the void center (Figure 2b). This relaxation of the host framework makes the two adjacent void spaces along the *c*-axis inaccessible, leading to an alternation of stuffed and empty cavities along **c**. The unstuffed cavities are occupied by the two Sn sites pushed together by contacts with the stuffing atoms in the neighboring cavities to form dumbells (Figure 2c).[35] This alternation of stuffing atoms and dumbbells along the *c*-axis is adhered to universally across the RET_6E_6 series.

Where the structural variability enters into the series is in the occupation patterns formed between neighboring voids along the *a*- and *b*-directions. Two archetypical patterns arise: For the $ScFe_6Ge_6$ structure ($HfFe_6Ge_6$-type), all columns are strictly

(33) Venturini, G. *J. Alloys Compd.* **2001**, *322*, 190–197.
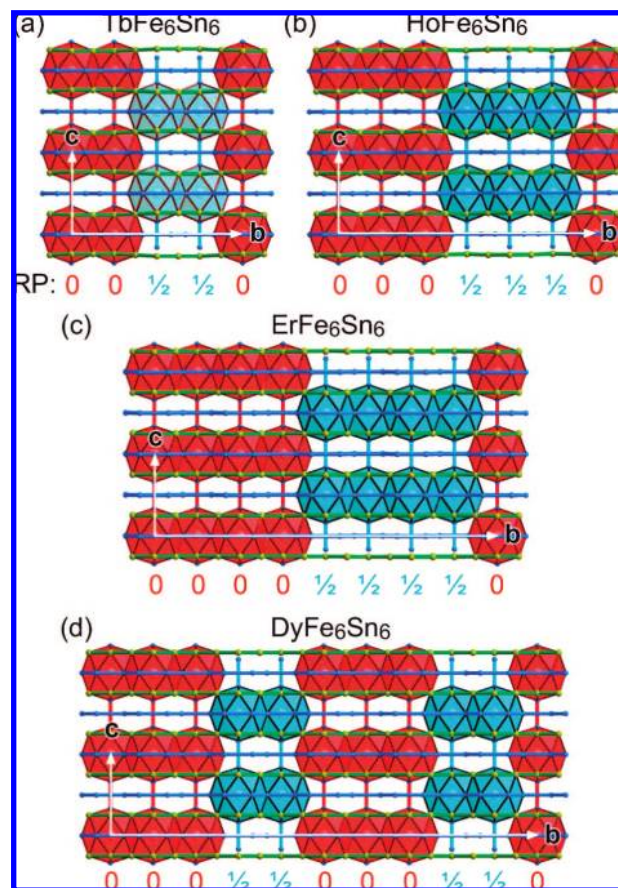(34) Venturini, G. *J. Alloys Compd.* **2001**, *329*, 8–21.
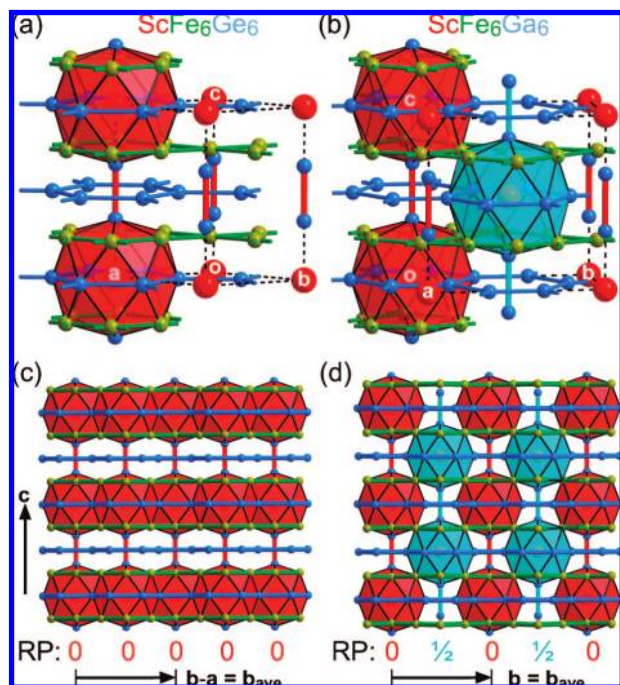
Figure 3. End-members in the $ScFe_6Ge_6$–$ScFe_6Ga_6$ intergrowth series. (a) The $ScFe_6Ge_6$ structure ($HfFe_6Ge_6$-type). (b) The $ScFe_6Ga_6$ structure. The coordination polyhedra of the Sc atoms are given in red and cyan for Sc atoms with z coordinates of, respectively, 0 and $1/2$. (c) In the $ScFe_6Ge_6$, all Sc atoms are at $z = 0$, 1, etc., creating layers of Sc polyhedra stacked along c. (d) In the $ScFe_6Ga_6$ structure, the Sc positions alternate between z coordinates of 0 and $1/2$ along the b-axis. RP: the relative position of the Sc atoms along the c-axis (see text). Intergrowth structures are generated by stacking blocks of these two structures along the b_{ave}-direction. For $ScFe_6Ge_6$, $\mathbf{b}_{ave} = \mathbf{b} - \mathbf{a}$ (in terms of the primitive hexagonal unit cell); for $ScFe_6Ga_6$, $\mathbf{b}_{ave} = \mathbf{b}$. Sc: red. Fe: green. Ga/Ge: blue.

in-phase giving rise to entire layers of stuffed or empty polyhedra (Figure 3a,c). For $ScFe_6Ga_6$, every other column is shifted half a unit cell along the c-axis, giving rise to rows of internally in-phase arrangements along the a-direction (Figure 3b,d). The other members of the structural series occur through the intergrowth of these two end-members, in which blocks of the $ScFe_6Ge_6$ structure are separated by antiphase boundaries taking the form of the $ScFe_6Ga_6$-type (see Figure 4 below). With the exception of the small number of compounds (ca. five) adopting the $ScNi_6Ge_6$- or $LiNi_6Ge_6$-types,[22] all of the ordered stuffed CoSn-type phases can be expressed as one of these intergrowths.

Over the course of this paper, we will draw out the reasons for the occurrence of these in-phase $ScFe_6Ge_6$-type blocks and their termination by $ScFe_6Ga_6$-type antiphase boundaries. We will develop this explanation over the next four sections, sections 2–5. Sections 2 and 3 treat the structures of the incommensurate members of the series. We begin (section 2) by extending the $ScFe_6Ge_6$–$ScFe_6Ga_6$ intergrowth scheme to incommensurate structures, encompassing the whole intergrowth series with a single 3 + 1D family. Section 3 demonstrates the practical utility

(35) In CoSn-type frameworks containing pnictogens, pnictogen–pnictogen dumbbells have been observed to spontaneously form, without the introduction of stuffing atoms. See: (a) Mills, A. M.; Lam, R.; Mar, A. *Can. J. Chem.* **1998**, *76*, 1558–1594; (b) Mills, A. M.; Mar, A. *J. Alloys Compd.* **2000**, *298*, 82–92. This suggests that the added valence electrons contributed by the electopositive stuffing atoms may promote dumbbell formation, in parallel with the necessity imposed by atomic size restraints. This is confirmed by inspection of crystal orbital overlap population curves, calculated with the extended Hückel method.

Figure 4. Examples of orthorhombic intergrowths of the $ScFe_6Ga_6$ and $ScFe_6Ge_6$ structure types, with the c-axis relative positions (RP) of the stuffing atoms given for each structure. (a) The $TbFe_6Sn_6$ structure. (b) The $HoFe_6Sn_6$ structure. (c) The $ErFe_6Sn_6$ structure. (d) The $DyFe_6Sn_6$ structure. See Figure 3 for color conventions.

of this higher-dimensional approach with the crystal structure refinements of incommensurate phases in the $ErFe_6(Ge/Ga)_6$ system from powder X-ray diffraction data. Important structural clues to the communication between host atoms can be identified in these structure solutions.

In section 4, we turn our focus to what drives these complex stuffing patterns. One important clue is the observation of a gradual shifting of the ordering patterns with incremental changes to the Ga/Ge ratios in the $REFe_6(Ge/Ga)_6$ (RE = Sc, Lu, Tb) systems.[20,33,34] This corresponds to a correlation between the superstructure and the electron concentration for these compounds. Such a dependence recalls the phenomena of Fermi surface nesting and the consequent charge density waves.[36,37] Instead, electronic structure calculations, at both *ab initio* and semiempirical levels, will demonstrate that incommensurability in this family derives from a fundamentally different source: a mutual antagonism between the energetic factors stabilizing the two end-members of the $ScFe_6Ge_6$–$ScFe_6Ga_6$ intergrowth series. The stabilities of the $ScFe_6Ge_6$- and $ScFe_6Ga_6$-types derive, respectively, from electrostatic and steric origins, which show opposite preferences regarding the simultaneous occupation of neighboring void spaces. A varying degree of balance in this tension creates the

(36) Wilson, J. A.; Di Salvo, F. J.; Mahajan, S. *Phys. Rev. Lett.* **1974**, *32*, 882–885.

(37) Canadell, E.; Whangbo, M.-H. *Chem. Rev.* **1991**, *91*, 965–1034.

intergrowth series. In the last major chapter of this paper, section 5, we use this model to explain structural trends within this family of compounds.

The ordering patterns in the stuffed CoSn-type family have quite intuitive origins, involving just the notions of tightly packed atoms repelling each other and cationic charges inducing enhanced anionic charges in their immediate neighbors (or alternatively: the shielding of cationic charges by electron redistributions in a metallic lattice). While the chemical bonding in intermetallic structures is intricate, the stories behind their superstructures do not have to be.

2. Superspace Model for the ScFe$_6$Ge$_6$–ScFe$_6$Ga$_6$ Intergrowth Structures

2.1. Commensurate Intergrowth Structures. The discovery of incommensurate phases in the ScFe$_6$Ge$_{6-\delta}$Ga$_\delta$ system makes a description of the entire ScFe$_6$Ge$_6$–ScFe$_6$Ga$_6$ intergrowth series as a single $3 + 1$ dimensional family appealing. A simple way to build such a description can be found from a close examination of the end-members themselves. These structures were shown in Figure 3. In both structures, hexagonal columns occur along the c-axis in which RE-filled void spaces alternate with dumbbell-filled void spaces. As we saw in the introduction, the major difference between the two structures occurs in the relative phases of this alternation in neighboring columns. For the ScFe$_6$Ge$_6$ structure, all the columns have the same phase, while in the ScFe$_6$Ga$_6$ structure, neighboring columns along the b-direction are out of step. These arrangements of the neighboring columns can be summarized with a simple notation that gives the relative position (RP) along the c-axis for each consecutive column along the b-axis. The ScFe$_6$Ge$_6$ structure follows the sequence ...0,0,0,0..., while ScFe$_6$Ga$_6$ follows the sequence ...0,$^1/_2$,0,$^1/_2$....

A number of intermediate structures, with other sequences, are known from other systems. Some examples are shown in Figure 4: in TbFe$_6$Sn$_6$ (*Amam*, Figure 4a), double rows of in-phase polyhedra are separated by antiphase boundaries to form a simple superstructure, ...0,0,$^1/_2$,$^1/_2$,0,0,$^1/_2$,$^1/_2$.... This can be extended to HoFe$_6$Sn$_6$ (*Immm*, Figure 4b), where the blocks are three rows wide (...0,0,0,$^1/_2$,$^1/_2$,$^1/_2$...) and ErFe$_6$Sn$_6$ (*Amam*, Figure 4c) with blocks four rows wide (...0,0,0,0,$^1/_2$,$^1/_2$,$^1/_2$, $^1/_2$...). A slightly more complicated structure is exhibited by DyFe$_6$Sn$_6$ (*Cmmm*, Figure 4d), where blocks three rows wide alternate with blocks two rows wide.

The generalization of this description to incommensurate structures is made simple if we exchange the discrete sequence of 0's and $^1/_2$'s for a periodic step function that alternates back and forth between the values 0 or $^1/_2$. This is illustrated in Figure 5a, where we show the ErFe$_6$Sn$_6$ structure (...0,0,0,0,$^1/_2$,$^1/_2$, $^1/_2$,$^1/_2$...) and plot below it an appropriate RP function. For the first four steps along the b-axis, the value of the function is 0, corresponding to no shift along the c-axis. For the next four steps, the function shifts to $^1/_2$ and then back to 0. The function is periodic with a period eight times the distance between columns along the b-axis, $\mathbf{b_{ave}}$. Along the b-axis, then, there are two periodicities at work: that of the displacement function (λ) and $\mathbf{b_{ave}}$.

This provides a general construction principle for the intergrowth family. We begin with a basic cell, metrically equivalent to the ScFe$_6$Ga$_6$ unit cell (or the *C*-centered orthohexagonal supercell of the hexagonal ScFe$_6$Ge$_6$ structure) but without the
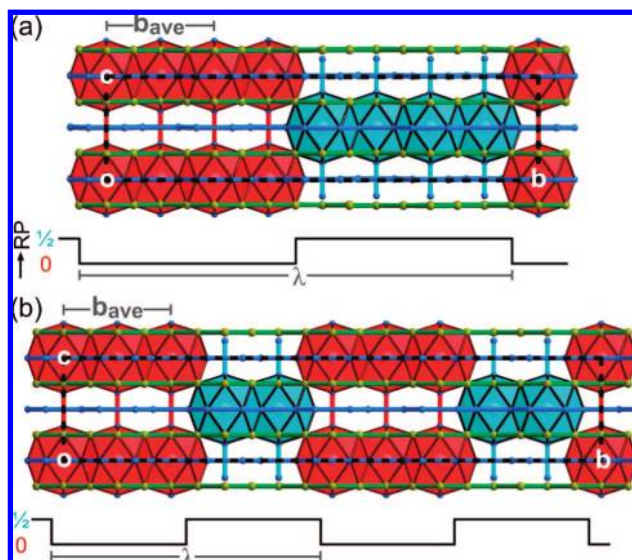
Figure 5. Construction of ScFe$_6$Ge$_6$–ScFe$_6$Ga$_6$ intergrowth structures, using a relative position (RP) function to give the c coordinates of the Sc stuffing atoms as a function of their position along the b-axis. The RP function is a periodic function, with period λ, and switches between values of 0 and $^1/_2$ at every interval of $\lambda/2$. (a) The ErFe$_6$Sn$_6$ structure ($n_{sc} = 4$, $\lambda = b$, i.e., $n_\lambda = 1$). (b) The DyFe$_6$Sn$_6$ structure ($n_{sc} = 5$, $\lambda = b/2$, i.e., $n_\lambda = 2$). See Figure 3 for color conventions.

stuffing atom/dumbbell occupation pattern specified. This pattern is then specified by imposing a RP position function on the structure.

Through the use of this construction, the full series of commensurate orthorhombic superstructures can be expressed using two parameters. The first is the number of $\mathbf{b_{ave}}$ repeats contained in the superstructure unit cell, which we will call n_{sc}, i.e. $n_{sc} = b/b_{ave}$. The second is the number of RP periods (λ repeats) in the supercell, $n_\lambda = b/\lambda$.

This is illustrated in Figure 5b for the DyFe$_6$Sn$_6$ structure, with $n_{sc} = 5$ and $n_\lambda = 2$. n_{sc} and n_λ values for other structures are tabulated in Table 1.

While these superstructures are most intuitively described by their real space geometries, the RP periods are usually detected in reciprocal space, through the inspection of X-ray diffraction patterns. These diffraction patterns are dominated by main reflections arising from the underlying basic cell, with satellite reflections arising from the presence of the antiphase boundaries imposed by the RP function. The main reflections can be indexed with the usual h, k, l indices, referring to the reciprocal lattice vector $h\mathbf{a}^* + k\mathbf{b_{ave}^*} + l\mathbf{c}^*$. Indexing the satellite reflections requires the introduction of a fourth reciprocal space basis vector, $\mathbf{q}$, so that the full pattern is indexed with four indices: h, k, l, m, which refer to the vector $h\mathbf{a}^* + k\mathbf{b_{ave}^*} + l\mathbf{c}^* + m\mathbf{q}$. For the commensurate structures we have looked at so far, the satellite reflections occur along the b^*-direction due to the antiphase boundaries being perpendicular to $\mathbf{b_{ave}}$. These satellites occur in the diffraction pattern at multiples of $\mathbf{q} = (0, q_y \cdot \mathbf{b_{ave}^*}, 0)$ from the main reflections, where q_y is b_{ave}/λ. As we can see from the full list of observed q-vectors in Table 2, the q-vector often exhibits a slight turning in the $\mathbf{a}^*$–$\mathbf{b_{ave}^*}$ plane. This lowers the symmetry of the resulting superstructures from orthorhombic to monoclinic.

2.2. Modeling Intergrowths in Superspace. Notice that the definitions of n_{sc} and n_λ in the previous section assume the existence of a periodic supercell. This breaks down when the repeat lengths of the RP function and the basic lattice become

Table 2. Observed q-Vectors in $ScFe_6Ge_6$–$ScFe_6Ga_6$ Intergrowth Structures, $\mathbf{q} = q_x \cdot \mathbf{a}^*_{ave} + q_y \cdot \mathbf{b}^*_{ave}{}^a$
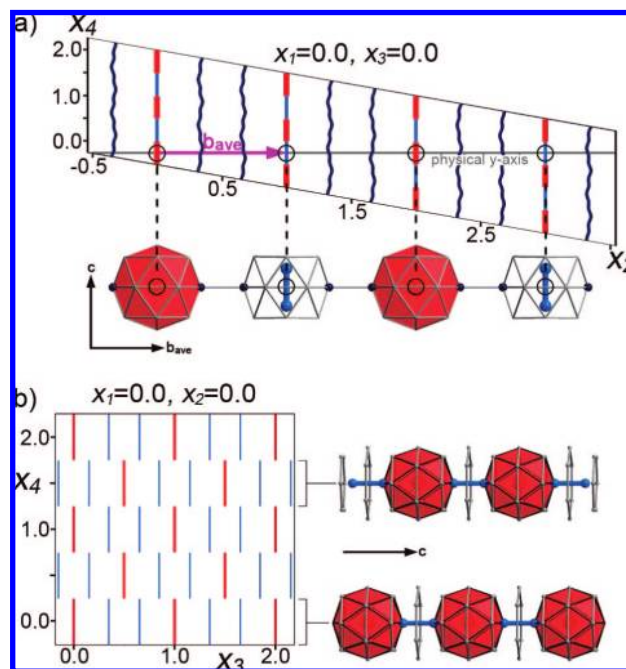
structure type	$|\mathbf{q}|/|\mathbf{b}^*_{ave}|$	q_x	q_y	ref
$HfFe_6Ge_6$	0.000	0	0	23
$ErFe_6Sn_6$	0.250	0	$1/4$	31
$ScFe_6Ge_{2.5}Ga_{3.5}$	0.273	0	$3/11$	33
$HoFe_6Sn_6$	0.333	0	$1/3$	31
YFe_6Sn_6	0.375	0	$3/8$	31
$DyFe_6Sn_6$	0.400	0	$2/5$	31
$TbFe_6Sn_6$	0.500	0	$1/2$	31
$ScFe_6Ge_{1.5}Ga_{4.5}$	0.569	0.0855	0.5495	33
$TbFe_6Ge_{4.25}Ga_{1.75}$	0.578	0.0795	0.5615	34
$LuFe_6Ge_{2.5}Ga_{3.5}$	0.596	0.0880	0.5760	20
$TbFe_6Ge_4Ga_2$	0.601	0.0875	0.5815	34
$LuFe_6Ge_2Ga_4$	0.660	0.1255	0.6235	20
$TbFe_6Ge_{3.5}Ga_{2.5}$	0.667	0	$2/3$	34
$TbFe_6Ge_3Ga_3$	0.706	0	$12/17$	34
$ScFe_6Ge_1Ga_5$	0.762	0.081	0.7490	33
$ScFe_6Ga_6$	1.000	0	1	24

^{a} For ease in comparison with the $ErFe_6(Ge/Ga)_6$ phases described in section 3, we have performed a transformation of the published unit cells for the monoclinic phases: keeping the q-vector direction and length fixed, we rotated the assignment of $\mathbf{a}_{ave}$ and $\mathbf{b}_{ave}$ by 60° about the c-axis, the pseudohexagonal axis of the underlying CoSn-type basic cell. With this choice of $\mathbf{a}_{ave}$ and $\mathbf{b}_{ave}$, the q_x value is minimized.

irrational with respect to each other; this is exactly the case in the incommensurate members of the stuffed CoSn-type family. With the onset of incommensurability in this family, we see vividly that these two period lengths show a high degree of independence from each other. A method for treating this independence explicitly is provided by the superspace formalism devised for incommensurately modulated structures. In this method, the x, y, z coordinates of each atom in the basic structure are mapped to the axes x_1, x_2, and x_3 of a 3 + 1D unit cell, while the RP function is laid out along the fourth axis, x_4 (illustrated schematically in Figure 6).

The coordinates within this 3 + 1D unit cell have a geometrically meaningful relationship to the atomic positions within the physical crystal. For the benefit of those interested in this structural family, but not specializing in incommensurate crystallography, we will briefly outline this relationship. Further details can be found in a variety of teaching and review articles.[38,39] First, let us stress the distinction between the 3 + 1D lattice and the physical crystal. By "physical crystal," we refer to the arrangements of atoms in 3D physical space, as they occur in the crystallites of our samples. By "3 + 1D lattice," we refer to a mathematical construction in 3 + 1D space from which a model for the atomic positions in physical space can be generated. For the series of structures described in this paper, three of the four dimensions of the 3 + 1D lattice describe the atomic positions within the basic unit cell of the series, while the fourth dimension gives the deviations from these average positions created by the relative position (RP) function described above.

In the physical, 3D, crystal the atoms occur at points with coordinates x, y, and z. With the introduction of the fourth dimension in the higher dimensional lattice, these points are stretched out into lines of the form $x_1(x_4)$, $x_2(x_4)$, $x_3(x_4)$, x_4, with x_4 representing the phase of the RP function. The function $x_1(x_4)$ describes how the x coordinate of an atom in the physical crystal varies with changes in the phase of the RP function, $x_2(x_4)$ the y coordinate, and $x_3(x_4)$ the z coordinate. Each (x_1, x_2, x_3) position

(38) van Smaalen, S. *Z. Kristallogr.* **2004**, *219*, 681–691.
(39) Petříček, V.; Dušek, M. *Z. Kristallogr.* **2004**, *219*, 692–700.

Figure 6. Schematic illustration of the features of the 3 + 1D unit cell for the $ScFe_6Ga_6$–$ScFe_6Ge_6$ intergrowth family. (a) The x_2–x_4 plane (with $x_1 = x_3 = 0$). The physical y-axis (gray line) occurs as a cut perpendicular to the x_4-axis. The tilting of the x_2-axis away from the y-axis leads to a shift in x_4 (the phase of the RP function) accompanying motions along y, and thus to the long-range occupation patterns of stuffing atoms and main group dumbbells in the CoSn-type framework's hexagonal cavities (bottom of (a)). Stuffing atom positions: red thick bars. Dumbbell centers: light blue bars. Atoms on walls of the hexagonal cavities: dark blue lines. (b) The form the RP function takes in the x_3–x_4 plane ($x_1 = x_2 = 0$). Stuffing atom positions (red vertical bars) and dumbbells (pairs of thinner blue vertical bars) alternate every half a unit cell along both x_3 and x_4.

along an atom's line represents a possible position for that atom in the crystal.

Creation of a 3D crystal from the 3 + 1D lattice proceeds through taking a slice through the higher-D lattice, cut perpendicular to the x_4 axis. The points of this higher-D plane coincide with the x, y, and z coordinates in the physical crystal. When, as in the incommensurate cases we have looked at so far, the RP phase depends only on the y coordinate ($\mathbf{q} = q_y \cdot \mathbf{b}^*_{ave}$), translations along the x and z directions lead to no change in the phase of the RP function (given by x_4). The corresponding axes in the higher-D cell, x_1 and x_3, are then perpendicular to x_4 and lie parallel to, respectively, the x and z axes. In other words, the independence in physical space of x, z, and the RP function phase appears in the 3 + 1D cell as a perpendicular relationship between the x_1 and x_4 axes and between the x_3 and x_4 axes (see Figure 6b).

For the more troublesome, incommensurate direction of the physical crystal, y, the situation is a little more involved. Translations along the y-direction create changes in both the position in the basic cell (x_2) and the phase of the RP function (x_4). This is accomplished through a tilting of the x_2 axis out of the cut through the 3 + 1D space which generates the physical crystal (Figure 6a). Thus if we start with a point in the physical crystal and make a translation of one unit cell along x_2, we move out of the physical crystal into the abstract higher-dimensional space. In order to stay in physical space, translations along x_2 must be coupled to a compensatory return to the physical crystal by a translation along x_4. This change in x_4 accompanying motion along x_2 produces the shift in the RP function phase

seen for translations of $\mathbf{b}_{\mathbf{ave}}$ in these structures. The magnitude of this x_4 shift for translating one unit cell along x_2 is the fraction of the RP function wavelength traveled by one $\mathbf{b}_{\mathbf{ave}}$ translation: $b_{ave}/\lambda = q_y$, where $\mathbf{q} = q_y \cdot \mathbf{b}_{\mathbf{ave}}^*$.

With the physical significance of the higher-dimensional coordinates in hand, we can easily, using our structural knowledge of the $ScFe_6Ga_6-ScFe_6Ge_6$ intergrowth series, create a model for the atomic positions within the higher-dimensional unit cell. We begin by placing all the atoms at fractional coordinates x_1, x_2, and x_3 equal to their fractional coordinates in the basic cell of the physical crystal. Along x_4 these atomic positions are stretched into straight lines, indicating that at this point the positions are independent of x_4.

Next, we note the major effect that the RP function has on the structure: this function orders the placement of stuffing atoms (RE) and main group dumbbells (E$-$E) into the hexagonal cavities of the CoSn-type framework. For any given point along the RP function, an alternation of stuffing atoms and dumbbells occurs along the z-axis (x_3-axis). Figure 6b shows how this is modeled in the 3 + 1D cell with an x_3 vs x_4 plot of the structure passing through the RE atoms and dumbbells ($x_1 = x_2 = 0$). The RE positions are drawn with thick red lines, and the E positions, with light-blue lines. For any given value of x_4, an alternation occurs along x_3 between RE positions and dumbbell positions.

In the commensurate phases we examined earlier, we saw that every half of an RP period the RE/E$-$E pattern is shifted by half a unit cell along the z-axis. This appears in the 3 + 1D cell as discontinuous interchanges of the RE and E$-$E positions as we move along x_4, with shifts happening every half of a unit cell along x_4. The overall arrangement is a checkered pattern, in which RE atoms and dumbbells alternate along both x_3 and x_4. One feature apparent here is a centering in this pattern: a $(0,0,^1/_2,^1/_2)$ translation leaves the pattern unchanged. This is, in fact, one of several 3 + 1D centering vectors belonging to the 3 + 1D superspace group symmetry of this family. In section S1 of the Supporting Information we give a derivation of the full superspace group symmetry for this family, which is described by 3 + 1D space groups $Xmmm(0\beta0)$ and $X2/m(\alpha\beta0)$ for the cases of, respectively, $\mathbf{q} = q_y \cdot \mathbf{b}_{\mathbf{ave}}^*$ and $\mathbf{q} = q_x \cdot \mathbf{a}_{\mathbf{ave}}^* + q_y \cdot \mathbf{b}_{\mathbf{ave}}^*$ (also included in section S1 is a translation of this space group notation for the uninitiated/bewildered).

In the structure refinements to come, this x_3-x_4 pattern is realized through the use of occupational modulation functions on the RE atom and E$-$E dumbbell positions, in which the RE position at ($x_1 = 0$, $x_2 = 0$, $x_3 = 0$) is fully occupied for the x_4 range $-0.25 \leq x_4 \leq 0.25$ and fully vacant for $0.25 \leq x_4 \leq 0.75$ (this step function in the occupation is known as a crenel function[40]). The dumbbell centered at ($x_1 = 0$, $x_2 = 0$, $x_3 = 0$) is complementarily modulated in occupation, with the dumbbell being fully absent for the x_4 range with the RE atom present ($-0.25 \leq x_4 \leq 0.25$) and occupied where the RE atom is absent ($0.25 \leq x_4 \leq 0.75$). The full pattern in the x_3-x_4 plane is then created from this through the $(0,0,1,0)$, $(0,0,0,1)$, and $(0,0,^1/_2,^1/_2)$ translations of the 3 + 1D lattice.

We have now captured with the higher-D model the connection between the RP phase (x_4) and the z coordinates of the RE atoms and E$-$E dumbbells. The 3D consequence of this pattern is seen when we move along the incommensurate direction of the crystal, y. The physical cut will pass through this x_3-x_4

pattern at varying x_4-values as y is traveled, generating the sequence of RP values of 0 and $^1/_2$.

This is pictured in Figure 6a, where we look onto the x_2-x_4 plane at $x_3 = 0$ and $x_1 = 0$. Here the physical y axis (gray line) runs perpendicular to x_4, and the tilting of x_2 with respect to y indicates that x_4 and x_2 have become entangled along this direction of the physical crystal. In this view, the RE atoms and E$-$E dumbbell centers share the same x_2 coordinate, and their alternation along x_4 appears as an alternation of red and light blue segments within single lines, which occur at every integer value of x_2 and intersect the physical y-axis at varying x_4 values. The resulting pattern of RE and E$-$E dumbbell occupations is shown schematically at the bottom of Figure 6a.

So far, we have considered only the most drastic of the structural changes created by the RP function: the placement of stuffing atoms and dumbbells. In addition to this, small changes in the surrounding framework might also be expected. The geometry of a RE-stuffed cavity probably varies a little from that of a dumbbell filled cavity. These variations in the framework positions occur in the higher-D cell as small variations in the atomic positions as a function of x_4. These positional variations can be modeled with a sum of harmonic functions, the coefficients of which can be introduced as parameters in crystal structure refinements. Such curves are visible for the E positions (dark blue lines) in Figure 6a.

Until now we have restricted ourselves to the case of modulated structures with orthorhombic symmetry. How will these considerations change for the monoclinic case (when $\mathbf{q} = q_x \cdot \mathbf{a}_{\mathbf{ave}}^* + q_y \cdot \mathbf{b}_{\mathbf{ave}}^*$)? The major change is that the RP function phase now evolves as we proceed down either the x or y directions of the crystal. In the higher-D cell, this means that both x_1 and x_2 are tilted out of physical space, and compensatory shifts along x_4 are needed for both if we are to stay in the physical crystal.

The new structural feature stemming from this is illustrated in Figure 7. First in Figure 7a, we show a typical orthorhombic case, that of $DyFe_6Sn_6$, and take a new view of the structure (lower panel of Figure 7a), looking down the c-axis to view the $\mathbf{a}-\mathbf{b}_{\mathbf{ave}}$ plane (to prepare for a turning of the q-vector in the $\mathbf{a}^*-\mathbf{b}_{\mathbf{ave}}^*$ plane). From this view, the alternation of regions with RP values of 0 and $^1/_2$ is most easily seen in the color-coding of the polyhedra: regions with RP = 0 appear as bands of red, with the RP = $^1/_2$ regions occurring as bands of cyan. These bands run perpendicular to the $\mathbf{b}_{ave}$-axis. A monoclinic case, that of $ErFe_6Ge_{6-\delta}Ga_\delta$, $\delta = 3.00$ (to be refined below), is shown in Figure 7b. As before, an alternation of bands in red and cyan occurs. This time, however, the bands are slanted with respect to the $\mathbf{b}_{ave}$-axis, due to the new dependence of the RP function phase on the coordinate along the a-axis.

In this section, we have outlined a superspace model for the $ScFe_6Ga_6-ScFe_6Ge_6$ intergrowth series. The major structural variation across the series, the allotment of RE stuffing atoms and E$-$E dumbbells, is produced from this model through simple changes in the degrees of tilting of the x_1 and x_2 axes out of the physical crystal. The more subtle features, such as relaxations within the hexagonal cavities, are then treated as small deviations from this starting point. In the next section, we will demonstrate this approach with the structure refinement of several new phases in the Er$-$Fe$-$Ge$-$Ga system, some of which are incommensurate.

(40) Petříček, V.; van der Lee, A.; Evain, M. *Acta. Crystallogr. A* **1995**, *51*, 529–535.
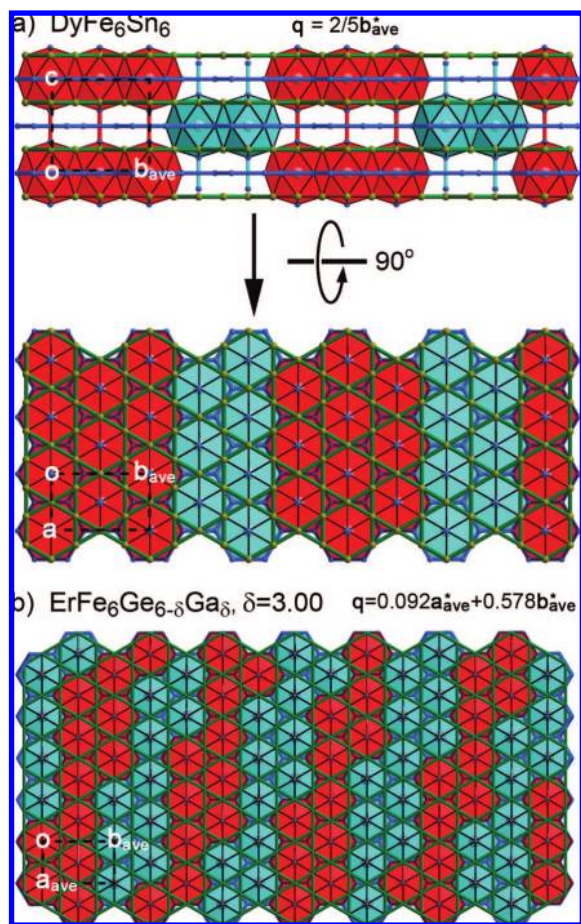
Figure 7. Structural effect of a turning of the q-vector in the $\mathbf{a}^*-\mathbf{b}^*_{ave}$ plane in the $ScFe_6Ga_6-ScFe_6Ge_6$ structural series. (a) In the $DyFe_6Sn_6$ structure, with its q-vector parallel to $\mathbf{b}^*_{ave}$, the RP function creates an alternation of sheets with RP = 0 (red) and RP = $^1/_2$ (cyan) running perpendicular to $\mathbf{b}^*_{ave}$. (b) For $ErFe_6Ge_{6-\delta}Ga_\delta$, δ =3.00, the q-vector has a component along $\mathbf{a}^*$ (now $\mathbf{a}^*_{ave}$, as this axis is now incommensurate). The result is that the RP = 0 and $^1/_2$ sheets are now slanted in the $\mathbf{a}_{ave}-\mathbf{b}_{ave}$ plane.

3. New Phases in the $ErFe_6Ge_{6-\delta}Ga_\delta$ Series

3.1. Overview of the $ErFe_6Ge_{6-\delta}Ga_\delta$ Series. In the above sections, we have surveyed the vast structural variety present in ternary stuffed CoSn-type frameworks, with compositions RET_6E_6 (RE = rare earth element or other electropositive cation, T = transition metal element, E = main group element), and have shown that this variety can be accounted for with a superspace model for the family. The structural versatility in this series is enhanced on going to pseudoternary systems by alloying two main group elements on the E sites. In the $ScFe_6Ge_{6-\delta}Ga_\delta$ series, for instance, the progressive substitution of Ge with Ga leads to an almost continuous shifting in the period of the RP function, with the resulting q-vector passing through incommensurate values. The ability to treat these incommensurate members of the family, alongside the conventional commensurate ones, is one of the chief advantages of the superspace treatment. In this section, we will demonstrate this in reporting the synthesis and crystal structure refinement of several phases in the Erbium series $ErFe_6Ge_{6-\delta}Ga_\delta$, where high-quality samples were obtainable.

In a survey of the $ErFe_6Ge_{6-\delta}Ga_\delta$ system, syntheses were carried out for several values of δ, and the resulting samples were examined with powder X-ray diffraction. Across the whole spectrum of nominal Ge/Ga compositions, the powder patterns

showed many commonalities. The patterns were dominated by strong reflections arising from the pseudohexagonal CoSn-type basic cells of the phases, with only small variations across the series. In addition to these, weaker satellite reflections appeared indicative of ordering in the Er stuffing atom positions. Also present are some prominent impurity peaks due to Er_2O_3. While the basic cell reflections showed only minor variations, changes in the Ge/Ga composition led to large changes in the satellites, in both position and, in some cases, peak width. In Table 3, we present examples of the phases detected in this survey. Over a large domain at the high Ge end of the series ($0.0 \leq \delta \leq$ ca. 2.8), the satellites can be indexed with a simple commensurate q-vector indicative of the $TbFe_6Sn_6$ structure type ($n_\lambda = 1$, $n_{sc} = 2$, $q_y = n_\lambda/n_{sc} = {}^1/_2$). With increasing Ga content, this gives way to two monoclinic incommensurate phases at $\delta = 3.00$ and $\delta = 3.25$, followed by a two-phase domain at $\delta = 3.50$ (not shown) containing one monoclinic and one orthorhombic phase. From $\delta = 3.75$ to 4.25, multiphase regions occur with broad satellites. Finally at the Ga-rich end of the series, $\delta = 4.50$, there is a return to commensurability with the simple $ScFe_6Ga_6$ structure type ($n_\lambda = 1$, $n_{sc} = 1$, $q_y = 1$).

The shifts in the satellite positions with changes in the Ge/Ga ratio are gradual enough that the evolution can be followed by comparison of powder patterns for neighboring values of δ. This is illustrated in Figure 8, where the powder patterns of four samples are shown over the small 2θ interval of about 35° to 42°, a range over which individual satellite reflections can be particularly well-resolved. The patterns for $\delta = 2.75$, 3.0, 3.25, and 4.5 are drawn in, respectively, black, blue, red, and green. In all of these patterns, the left and right sides of the figure are bordered with high-intensity peaks, arising from the basic cell. In between these main reflections, in the range 36° to 41°, less intense reflections are visible. Large dots trace out the evolution of one set of satellites, those with the indices $(h,k,l,m) = (1,1,3,-1)$ and $(1,-1,3,1)$.

At $\delta = 2.75$, the orthorhombic symmetry of the $TbFe_6Sn_6$ structure type leads to an *mmm* point symmetry of the diffraction pattern, which in turn makes the $(1,1,3,-1)$ and $(1,-1,3,1)$ reflections symmetry equivalent. The result is a single peak, marked by a single black dot. At $\delta = 3.00$, the symmetry lowering to monoclinic symmetry is evident by the splitting of the $(1,1,3,-1)$ and $(1,-1,3,1)$ reflections into slightly lower- and higher-angle reflections (blue dots), respectively. This splitting is widened on going to $\delta = 3.25$ (red dots). At $\delta = 4.50$, orthorhombic symmetry is restored with the coalescence of $(1,1,3,-1)$ and $(1,-1,3,1)$ into a single peak.

While the splitting of these two reflections makes it easy to monitor the breaking and recovery of orthorhombic symmetry, it obscures how the length of the q-vector changes in the process. To show the variation in q-vector length, as well as provide a more visual interpretation of this satellite motion, we give as an inset in Figure 8 a schematic view of the reciprocal lattice for these phases. We draw with gray circles the reciprocal lattice points of the basic cell in the $(h, k, l = 3)$ layer, or in the $3 + 1D$ indexation scheme: $(h, k, l = 3, m = 0)$. These reflections are all absent due to the $l + m = 2n$ condition from the X-centering. Then, with colors matching the powder patterns in the main figure, we plot out the positions of the first-order satellites corresponding to the dots in the powder patterns, $(1,1,3,-1)$ and $(1,-1,3,1)$. For $\delta = 2.75$, the satellites (black) are aligned with $\mathbf{b}^*_{ave}$ and lie halfway between basic cell reflections, as expected for the twofold superstructure exhibited by the $TbFe_6Sn_6$-type. Because these two satellites are related

Table 3. Rietveld Refinement Parameters and Results for $ErFe_6Ge_{6-\delta}Ga_\delta$ Samples[a,b]

	$\delta = 2.50$	$\delta = 3.00$	$\delta = 3.25$	$\delta = 4.50$
basic cell				
a_{ave} (Å)	5.0676(2)	5.0600(3)	5.0582(4)	5.0582(2)
b_{ave} (Å)	8.7542(4)	8.7492(5)	8.7490(7)	8.7148(4)
c (Å)	8.2910(3)	8.3155(3)	8.3311(3)	8.4087(4)
α (deg)	90	90	90	90
β (deg)	90	90	90	90
γ (deg)	90	90.069(4)	90.088(5)	90
V (Å^3)	367.81(4)	368.13(4)	368.68(4)	370.66(4)
3 + 1D space group	$Xmmm(0\beta0)000$	$X2/m(\alpha\beta0)00$	$X2/m(\alpha\beta0)00$	$Xmmm(0\beta0)000$
$q = q_x\mathbf{a_{ave}^*} + q_y\mathbf{b_{ave}^*}$	$q_x = 0$	$q_x = 0.0920(2)$	$q_x = 0.1221(3)$	$q_x = 0$
	$q_y = 0.5$	$q_y = 0.5783(4)$	$q_y = 0.6226(4)$	$q_y = 1$
λ (Å)	17.508	14.582	13.301	8.715
refinement details				
$R(I > 3\sigma)$	4.83	4.79	5.58	4.49
$R_w(I > 3\sigma)$	3.58	2.65	2.57	2.60
R_{wp}	2.01	1.71	1.71	1.77

[a] δ values for the $ErFe_6Ge_{6-\delta}Ga_\delta$ phases reported in this paper refer to the nominal compositions of syntheses, as opposed to parameters in the structure refinements. [b] An extended version of this table is presented as Table S2 in the Supporting Information.
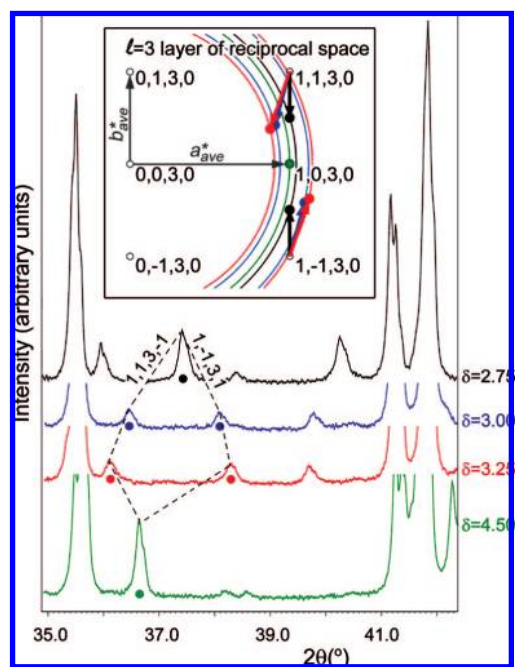
Figure 8. X-ray diffraction data of $ErFe_6Ge_{6-\delta}Ga_\delta$ samples over one 2θ window displaying individually discernible satellites. Black, $\delta = 2.75$; Blue, $\delta = 3.0$; Red, $\delta = 3.25$; Green, $\delta = 4.5$. Circular dots indicate the peaks arising from the reflections $(h,k,l,m) = (1,1,3,-1)$ and $(1,-1,3,1)$. Inset: a schematic illustration of the $l = 3$ layer of the reciprocal lattice provided for interpretation of the peak positions in the diffraction data. Gray open circles mark the reciprocal lattice points of the basic cell, i.e. $(h, k, l = 3, m = 0)$ reflections. Circular dots give the positions of the $(1,1,3,-1)$ and $(1,-1,3,1)$ reflections; these are color-coded to match their corresponding peaks in the powder patterns below. Thick arrows trace the displacement of the satellites from their associated main reflections. Portions of circles centered around $(0,0,3,0)$ are drawn to aid the eye in comparing the distances of the satellites from the origin, the factor determining the diffraction angle of a reflection.

by a mirror operation passing through the origin perpendicular to $\mathbf{a_{ave}^*}$, they are equidistant from the origin. Thus they correspond to the same d-spacing and diffraction angle and, thus, contribute to the same peak in the powder diffraction pattern. We highlight this in the inset by showing that both points lie on the same circle around the origin, on which all points map to the same angle in the diffraction pattern.

As we move to $\delta = 3.00$ (blue), two changes in the q-vector are visible in the inset. Most obvious is the turning of the q-vector out of alignment with $\mathbf{b_{ave}^*}$ in the $\mathbf{a_{ave}^*}-\mathbf{b_{ave}^*}$ plane. In this process, the $(1,1,3,-1)$ position turns *toward* the origin, while the $(1,-1,3,1)$ position turns *away* from it, breaking the mirror symmetry connecting the two reflections. They now have different distances from the origin (as indicated by the two blue circles). This inequality leads to a visible splitting of these reflections in the powder pattern. In addition to this turning, the q-vector undergoes a lengthening relative to the $\delta = 2.75$ case. The same features occur for the $\delta = 3.25$ q-vector (red). Here, the turning is sharper leading to a greater splitting between $(1,1,3,-1)$ and $(1,-1,3,1)$, and the q-vector is further lengthened.

A sharp change occurs when we move to $\delta = 4.50$. Here the q-vector snaps back into axial alignment with $\mathbf{b_{ave}^*}$ and lengthens to the point where it is equal in length to $\mathbf{b_{ave}^*}$. Thus we have come to a perfectly commensurate case where steps in reciprocal space by $\mathbf{b_{ave}^*}$ are indistinguishable from translations by the q-vector. In this case, the $(1,1,3,-1)$ and $(1,-1,3,1)$ positions now both lie on the basic cell reciprocal lattice point $(1,0,3,0)$. This position is plotted in the inset with a green dot, which corresponds to a single position in the diffraction pattern.

While the evolution of the q-vector seems rather discontinuous across this series, several continuous changes can be discerned across this series (Table 3). In the cell parameters of the basic cell, increasing Ga content produces a gradual expansion of $\mathbf{c}$ coupled with contractions in $\mathbf{a_{ave}}$ and $\mathbf{b_{ave}}$. The net effect is an increase in the volume of the basic cell, as expected for the substitution of Ge with the larger Ga. There is also a trend in the length of the RP function repeat, λ, which shrinks monotonically across the series. In the following, we will discuss the structures of these phases, as elucidated through Rietveld refinements.
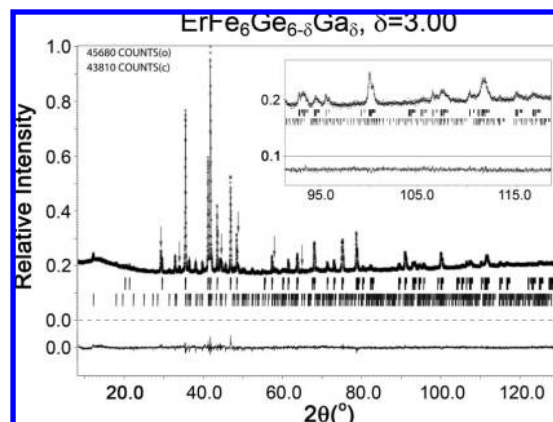
3.2. Crystal Structures of the $ErFe_6Ge_{6-\delta}Ga_\delta$ Phases. The structural refinement of the second phase in Table 3, $ErFe_6Ge_3Ga_3$, proved particularly simple and provides a friendly starting point for discussing how these refinements were made and the information that can be extracted from them. Let us start with a short overview of the refinement process. It began with a preliminary step in which the background correction parameters, zero-offset, cell parameters, q-vector, and profile

parameters were optimized using the Le Bail refinement[41] feature of the JANA2000 package.[42] In this step, the necessity of including impurity phases Er_2O_3 and $Fe_{13}Ge_8$ became apparent (see Table S2 of the Supporting Information).

Once these powder parameters converged and examination of the Bragg positions and profiles indicated that the peaks were being well-modeled, the refinement of the $ErFe_6Ge_3Ga_3$ crystal structure began. As the q-vector for this phase is monoclinic, we used the superspace group $X2/m(\alpha\beta0)00$ (see section S1 in the Supporting Information for the derivation of this space group symmetry). For our starting model, we put Er, Fe, and Ge/Ga atoms at their respective positions within the basic cell. These are labeled Er1 for the stuffing atom, Fe1a−Fe2 for the Fe kagomé layer positions, Ge1 for the single symmetry-distinct site on the Ge/Ga honeycomb net, and Ge2 for the Ge/Ga dumbbell position (details can be found in Table S3 of the Supporting Information). Also included in the starting model are the crenel occupational functions on the Er1 stuffing atom and Ge2 dumbbell atom positions. For the Ge/Ga positions, we simply used a Ge structure factor, as the similarities in electron count between Ge and Ga make their distinction difficult. From this starting point, the scale factor and phase volumes were refined, along with the positions of the atoms within the basic cell. Refining these parameters alone leads to rather good R-factors for both main reflections and first-order satellites (main reflections, $R_1(I > 3\sigma) = 3.05$; first-order satellites, $R_1(I > 3\sigma) = 10.12$) as well as for the profile fitting ($R_{wp} = 1.80$).

Following this, harmonic positional modulation functions were gradually added, leading to small improvements in the R-factors. In recognition of the limitations of our powder data, we then culled those modulation waves with coefficients not significantly different from zero. Inclusion of second-order modulations did not lead to convincing improvements in the R-factors. In the end, only three atoms were modeled with positional modulations: the Er1 stuffing atom, the Ge1 honeycomb, and the Ge2 dumbbell positions. Refinement of the Er1, Ge1, and Ge2 positional modulation wave coefficients brought modest improvements to the R-factors (main reflections, $R_1(I > 3\sigma) = 2.56$; first-order satellites, $R_1(I > 3\sigma) = 8.81$; profile fit, $R_{wp} = 1.71$). More details on the results of the refinement can be found in Tables S2 and S3 in the Supporting Information. The experimentally measured intensities are compared to the calculated ones in Figure 9. While there are some small features apparent in the difference curve, it is predominantly flat. A comparison with the Bragg positions and powder pattern reveals that the biggest features in the difference curve occur at relatively large diffraction peaks arising from the main reflections.

Having discussed the refinement procedure and reliability of the results, we can now turn to the structure itself. The q-vector emerging from the refinement has sizable components along both the a_{ave}^*- and b_{ave}^*-directions: $\mathbf{q} = 0.0920\mathbf{a}_{ave}^* + 0.578\mathbf{b}_{ave}^*$. Thus in the physical crystal the phase of the RP function will depend on an atom's position along both the a_{ave}- and b_{ave}-axes. Also, the q-vector's coefficients along both axes are far from any ratio of small integers, and thus the structure is most conveniently and convincingly treated as incommensurate. As such, a comprehensive picture of the structure cannot be made with a finite 3D model. However, a large sample of the structure

(41) Le Bail, A.; Duroy, H.; Fourquet, J. L. *Mater. Res. Bull.* **1988**, *23*, 447−452.

(42) Petříček, V.; Dušek, M.; Palatinus, L. *Jana 2000. The Crystallographic Computing System*; Institute of Physics: Praha, Czech Republic, 2000.

Figure 9. Powder X-ray diffraction data for $ErFe_6Ge_3Ga_3$, overlaid with the calculated pattern from the Rietveld refinement. Vertical bars give the refined Bragg positions for main reflections (top row) and first-order satellites (bottom row). Longer bars: reflections from Cu Kα_1 radiation. Shorter bars: from Cu Kα_2. Gray arrows: prominent features due to Er_2O_3 or $Fe_{13}Ge_8$ impurities. The difference curve is drawn to scale with respect to the calculated and observed patterns.

provides a general idea of the features it exhibits. In Figure 10b, we draw out a $7\mathbf{b}_{ave} \times 5\mathbf{a}_{ave}$ region of this structure. As in Figure 7b, the values of the RP function are represented with the colors of the Er polyhedra: red for RP $= 0$, cyan for RP $= 1/2$. The RP $= 0$ and $1/2$ regions again form bands which are slightly inclined from the a_{ave}-direction. The repeat vector of the RP function, $\boldsymbol{\lambda}$ (white arrow), runs perpendicularly to these bands ($\boldsymbol{\lambda}$ is the real-space counterpart to the q-vector; it is parallel to $\mathbf{q}$, with the magnitude $1/|\mathbf{q}|$).

The RP function pattern has a close relationship to the $TbFe_6Sn_6$-type structure shown in Figure 10a (exemplified here by an Er−Fe−Ge−Ga phase discussed further below). This simpler structure consists of an alternation along the b_{ave}-axis of two-polyhedron-thick RP $= 0$ slabs with RP $= 1/2$ slabs of the same thickness. In $ErFe_6Ge_3Ga_3$ (Figure 10b) fragments of such slabs can be seen, but they are broken up, with the double columns of RP $= 0$ or RP $= 1/2$ interrupted by slips in the RP phase diagonal to the a_{ave}- and b_{ave}-axes. For the most part, the slab fragments are three $\mathbf{a}_{ave}$ repeats long, but shorter ones are also visible in this view.

A more comprehensive view of the structure, one that is not limited to local regions of the crystal, can be obtained by examining the positions of the atoms in the superspace unit cell, where the structure is periodic. It is particularly informative here to plot the four-dimensional electron density constructed by Fourier synthesis using the reflection intensities from the powder diffraction data and phases calculated from the structure model (F_{obs} densities). Comparison of this electron density with the model positions provides a further measure of how consistent the structural model is with the diffraction data and provides directly hints of where the model can be improved. The F_{obs} density maps for the key sections of the $3 + 1D$ unit cell discussed earlier (Figure 6) are shown in Figure 11a,b.

Figure 11a illustrates the effect of the RP function phase (x_4) on the placement of the Er1-stuffing atoms and Ge2 dumbbells along the c-direction. The model positions for these atoms are drawn with thick red bars and thinner light-blue bars, respectively. The pattern is the same as that we saw earlier in Figure 6: an alternation of Er1 and Ge2 dumbbell positions every half of a unit cell along both x_3 and x_4. Below these bars, F_{obs} electron density contours for the $x_1 = x_2 = 0$ layer are plotted. Regions
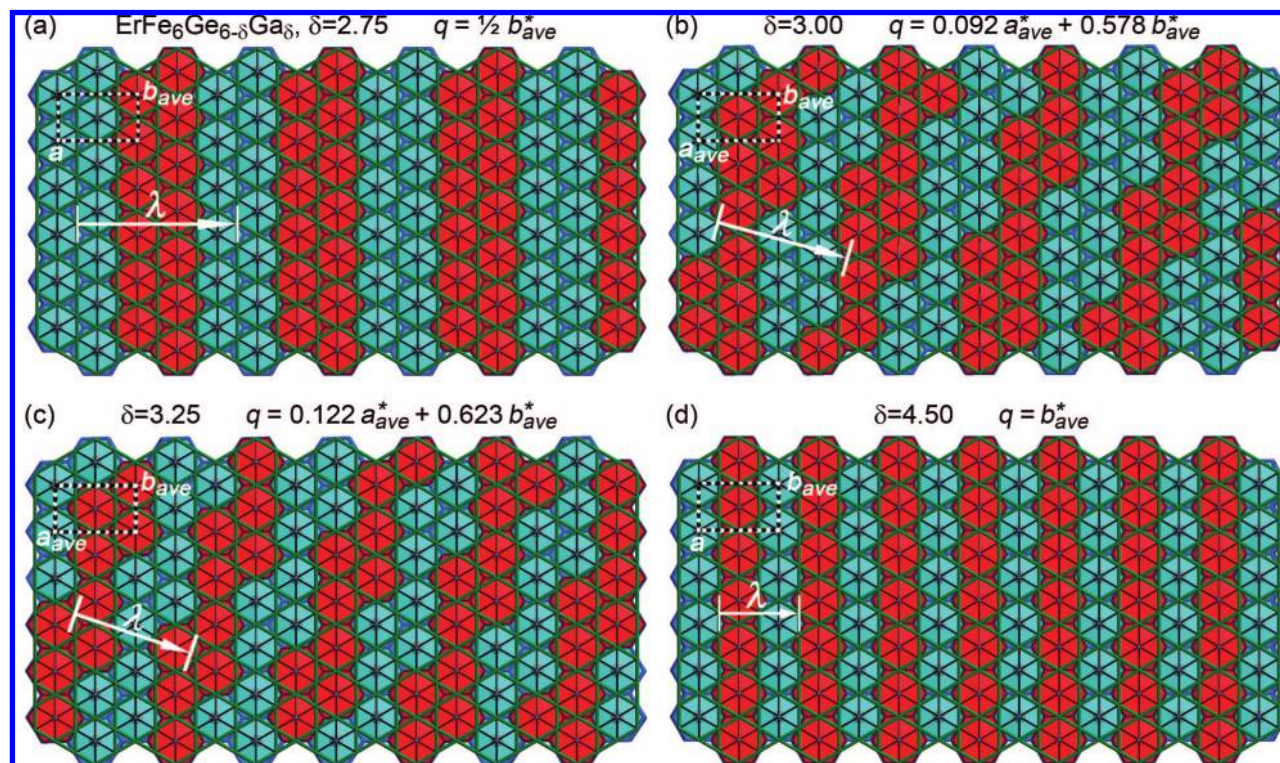
Figure 10. Survey of $ErFe_6Ge_{6-\delta}Ga_\delta$ crystal structures refined in this work: (a) $\delta = 2.75$, (b) $\delta = 3.00$, (c) $\delta = 3.25$, and (d) $\delta = 4.50$. Red polyhedra correspond to Er atoms with RP = 0, cyan with RP = $^1/_2$ (see Figure 7). For each structure, the basic cell and RP repeat vector, λ, are shown. In each picture, the λ-vector is drawn at the same starting point. Thus the length and direction of λ for different δ-values can be qualitatively compared using the various types of hexagonal nets arising from the basic cell as references. Note that because the structures in (b) and (c) are incommensurate, such depictions can provide only local views of the structures, not crystallographically repeating units.

of high electron density occur beneath each of the Er1 and Ge2 bars, and the remainder of the map is largely featureless. The termination of the electron density near the tips of the bars along x_4 supports the crenel nature of the occupational modulations in this structure. Also reproduced in the contours is the difference in electron count between the Er1 and Ge2 atoms: many more contour lines have collected under the Er1 bars than under the Ge2 ones.

While the x_3-x_4 map in Figure 11a shows that the Er1/Ge2 dumbbell alternation has been well-modeled, we need to take another view to see how the rest of the structure responds to this pattern. The largest response, that of the Ge1 atoms, can be seen in the x_2-x_4 cross section passing through the Er atoms (at $x_1 = x_3 = 0$), as presented in Figure 11b. In this map, the model's positions for the Er1 atoms, Ge2 dumbbell centers, and Ge1 atoms are again drawn with color-coded lines (thick red, lighter blue, and darker blue, respectively). The Er1 and Ge2 positions again alternate along x_4, with the Er1 bars slightly tilted, reflecting a slight positional modulation. The Ge1 positions occur as smoothly varying harmonic waves rippling down x_4. The contours of the F_{obs} electron density in this layer (with a summation over a small width in x_1, see figure caption) match these features of the model, with large densities pooled beneath the Er1 positions, no appreciable density at the centers of the Ge2 dumbbell, and waving streams of density following the Ge1 curves.

From this diagram, we can also see how the Ge1 modulation is tuned to the Er1 atom/Ge2 dumbbell alternation. To do this, we recall that we go from the $3 + 1D$ structure to the 3D one by taking cuts perpendicular to the x_4-axis. To see which points in this x_2-x_4 plane will occur together in the physical crystal,

we should then draw a line perpendicular to x_4; neighboring atomic positions along such a line are also neighboring in the 3D space. Two such cuts are sketched in with gray dotted lines in Figure 11b, one for an Er1 position and one for a Ge2 position. Both positions are placed between two Ge1 positions, which form part of the hexagonal polyhedron housing each stuffing atom and dumbbell (see Figure 2). The spacing of Ge1 positions around the Er1 and Ge2 positions are unequal; undulation of the Ge1 position serves to shrink the space around the Ge2 dumbbell centers and expand the space around the Er1 positions. This tendency can be understood from size considerations. If an Er atom requires more space than the meeting point of two Ge atoms, then just as a belt is loosened or tightened around wider or thinner waists, respectively, the hexagons of the Ge1 honeycomb layers expand around the Er stuffing atoms and contract around the Ge2 dumbbells.

Figure 11c illustrates the consequences of this Ge1 modulation in physical space. A single Ge1 honeycomb layer is drawn along with the Er1 atoms that populate it. The honeycomb layer is strikingly close to ideal. In order to clearly represent the deviations in the layer, arrows have been added to indicate the magnitude and direction for each of the larger displacements (>0.08 Å). The arrow lengths are scaled to be 30 times the actual deviation. Even if the distance each Ge1 atom travels under this modulation is small, the orientations of the arrows show a clear trend: they point away from the Er-filled hexagons into empty hexagons, again suggesting that Ge1 atoms move to provide more space around the Er atoms. Further support for this interpretation is provided by the close alignment of the Ge1 displacement arrows with the RP repeat vector, λ (drawn in green). While the x- and y-coefficients of the Ge1 harmonic
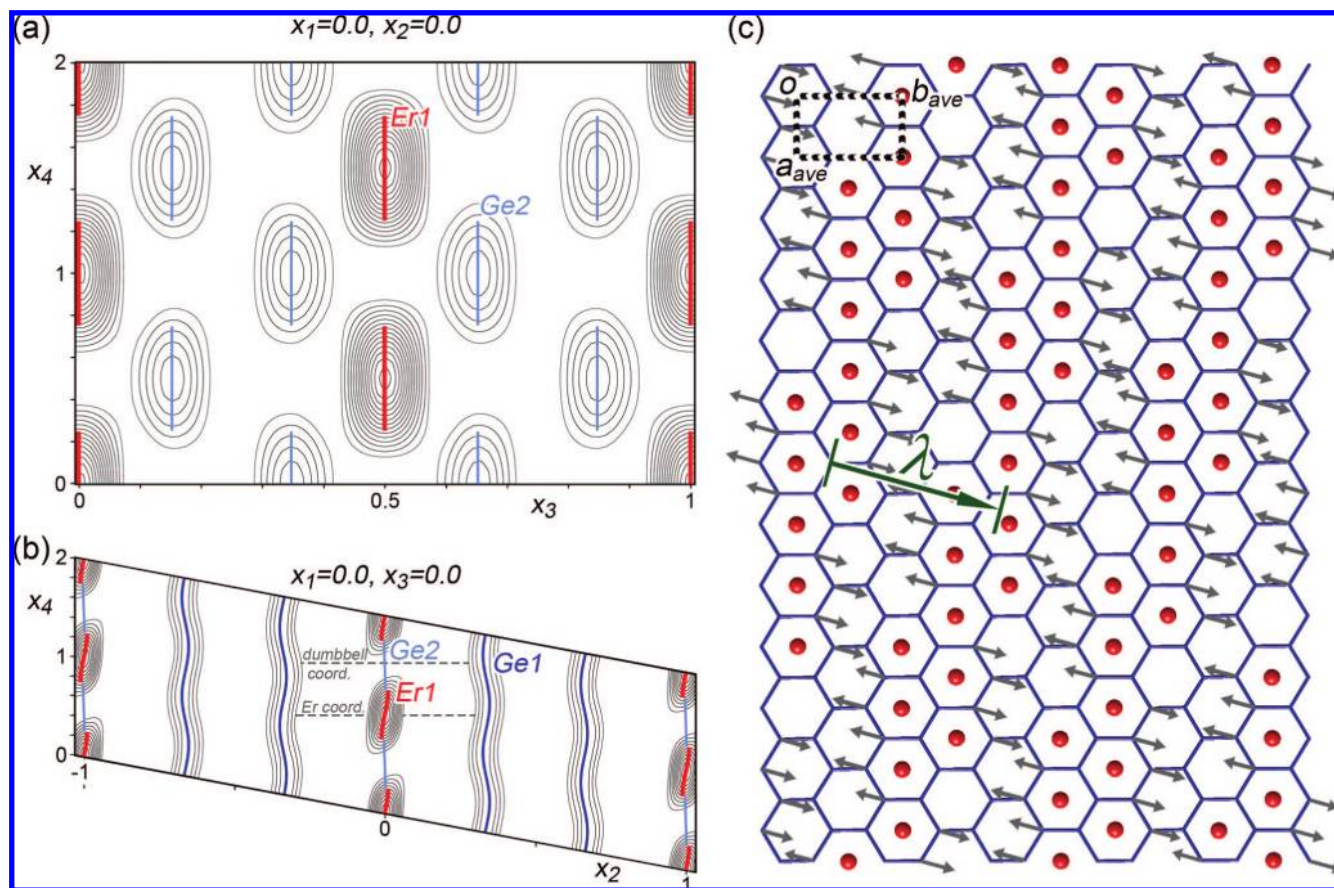
Figure 11. Analysis of the refinement results for $ErFe_6Ge_3Ga_3$. (a) Contour map of the electron density in the x_3-x_4 plane passing through the Er stuffing atoms (see Figure 6), calculated by Fourier synthesis using intensities extracted from the diffraction data and phases calculated from the structural model (F_{obs} map). Note the correspondence in both position and size of the electron density with the model's positions for the Er (thick, red bars) and Ge2 dumbbell (thinner, light blue bars) atoms. (b) F_{obs} map for the x_2-x_4 plane centered on the Er atoms. The electron density is summed over a small thickness in the x_1 direction to fully capture the Ge1 atoms (darker blue) which show a small deviation from $x_1 = 0$. No significant electron density is expected in this map at the Ge2 positions, as this plane cuts between the atoms of the dumbbells, not through the atoms themselves. Dotted lines trace out the local coordination of one Er and one dumbbell position by Ge1 atoms along the physical y axis. The Ge1 position is modulated in response to the Er atom/dumbbell occupation pattern: as can be seen from the lengths of the dotted lines, the Ge1 modulation opens space around Er1 positions, and contracts around the dumbbells. (c) The distortions of the Ge1 honeycomb nets resulting from this modulation. One Ge1 honeycomb layer is shown, along with the Er stuffing atoms lying in it (red spheres). For each Ge1 displacement larger than 0.08 Å, the displacement vector is drawn with a gray arrow, with the arrow length equal to 30 times the displacement. In green is drawn the repeat vector of the RP function, λ.

modulations have not been constrained in any way, they have converged to values leading to displacements virtually parallel to the λ-vector. This parallel alignment allows the Ge1 displacements to be normal to the interface between RP = 0 and $^1/_2$ regions. This ensures that the motion of one Ge1 atom to elongate an Er1—Ge1 contact does not shorten another Er1—Ge1 contact in the process.

In summary, the implementation of the superspace model for the stuffed CoSn-type series of structures allowed for the refinement of the incommensurate $ErFe_6Ge_3Ga_3$ phase from powder X-ray diffraction data. A rather good fit to this data was provided by a simplistic model in which the Er stuffing atom and Ge/Ga dumbbell RP function is imposed without any subsequent relaxation of the surrounding structure (main reflections, $R_1(I > 3\sigma) = 3.05$; first-order satellites, $R_1(I > 3\sigma) = 10.12$; profile fit, $R_{wp} = 1.80$). The addition of positional modulation parameters allowed the resolution of some small relaxations in response to the occupation pattern created by the RP function. Chief among these is a modulation in the Ge1 honeycomb site which expands the hexagonal void spaces around the Er stuffing atoms and contracts the voids around the Ge/Ga dumbbells. Inclusion of these small modulations leads to correspondingly

small improvements in the R-factors (main reflections, $R_1(I > 3\sigma) = 2.56$; first-order satellites, $R_1(I > 3\sigma) = 8.81$; profile-fit, $R_{wp} = 1.71$).

Aside from the ease of the refinement procedure, two further advantages of this superspace method become evident in this analysis. One is the intimate connection between the structural parameters and the structural interpretation. As each modulation wave describes a periodic, geometrically meaningful distortion of the structure, simply stating the amplitudes and geometrical natures of these waves provides a vivid description of a three-dimensionally aperiodic crystal. The second advantage is related: the depiction of the structure with only a small number of coefficients and average positions allows for great economy in the number of parameters used in the refinement. In the refinement of $ErFe_6Ge_3Ga_3$, only 11 parameters were required for specifying the atomic positions. As can be seen in the other $ErFe_6Ge_{6-\delta}Ga_\delta$ phases to come, the number of parameters can be further reduced without significant sacrifices in the quality of the refinement, as judged from the R-factors or inspection of F_{obs} maps.

The refinements of the remaining Er—Fe—Ge—Ga phases in Table 3 proceeded with only small variations on that of the δ

= 3.0 phase just described (details can be found in section S2 of the Supporting Information). The results of these refinements are summarized in Tables S2 and S3, and views of the emerging structures are presented in Figure 10. The full series of structures adhere to the same structural themes observed for the $\delta = 3.0$: a full ordering of the Er1 stuffing atoms and Ge2 dumbbell atoms is detected for each phase. Relaxations in the surrounding framework accompanied this ordering, with the chief distortion being relative expansion and contraction of the Ge1 honeycomb nets around, respectively, the Er1 atoms and Ge2 dumbbells.

3.3. ErFe$_6$Ge$_{6-\delta}$Ga$_\delta$ Structures in Context. The q-vector shows a complicated progression across the system, with both its length and direction being functions of δ. A sequence of commensurate and incommensurate, orthorhombic and mono-clinic structures results. While this sequence seems complex, it becomes more intuitive when we place it in the context of the larger family of ScFe$_6$Ge$_6$−ScFe$_6$Ga$_6$ intergrowth structures. In Table 2 we tabulated all of the previously observed intergrowth structure types, giving for each phase the q_x and q_y components of its q-vector and the q-vector's length relative to the $\mathbf{b}_{ave}^*$ basic cell vector, $q_{rel} = |\mathbf{q}|/|\mathbf{b}_{ave}^*|$. Taking the full range of structures together, we see that the turning of the q-vector occurs in specific ranges along the progression between the ScFe$_6$Ge$_6$ ($q_x = 0$, $q_y = 0$) and ScFe$_6$Ga$_6$ ($q_x = 0$, $q_y = 1$) structure types. The range of q-vector lengths $0 \leq q_{rel} \leq {}^1/_2$ is populated exclusively by orthorhombic structures, with $q_x = 0$. This is followed by a region from $q_{rel} = {}^1/_2$ up to roughly ${}^2/_3$, over which a small q_x component appears, indicating the structures are monoclinic. Between the end of this monoclinic region up to the ScFe$_6$Ga$_6$ end-member, ${}^2/_3 \leq q_{rel} \leq 1$, only a few structure types have been discerned, two orthorhombic and one monoclinic.

The structural progression determined above for the ErFe$_6$Ge$_{6-\delta}$Ga$_\delta$ system fits well into the $q_{rel} = {}^1/_2$ to 1 portion of this scheme. For $\delta = 2.75$, the phase crystallizes as the orthorhombic $q_x = 0$, $q_y = {}^1/_2$ (TbFe$_6$Sn$_6$) structure type. This lies directly at the border between the orthorhombic and monoclinic regions in Table 2. Upon increasing δ further, the length of the q-vector increases, and as expected a switch to monoclinic structures occurs. At $\delta = 3.00$ the q-vector has the components $q_x = 0.092$ and $q_y = 0.578$, and moving to $\delta = 3.25$, the monoclinicity continues with $q_x = 0.122$ and $q_y = 0.622$. Moving to higher Ga content, $\delta = 3.50$ produces a two-phase sample with nearly commensurate q-vectors for both phases. One phase is monoclinic with its q-vector very close to $q_x = {}^1/_8$, $q_y = {}^5/_8$. The second phase is orthorhombic, with the q-vector close to $q_x = 0$, $q_y = {}^2/_3$. The q_{rel} values of, respectively, 0.661 and 0.667 coincide with the end of the $q_{rel} = {}^1/_2$ to ${}^2/_3$ monoclinic region in Table 2. The $\delta = 3.50$ two-phase sample thus straddles the border between the high-q_{rel} end of the monoclinic region and the reemergence of orthorhombic phases. The $\delta = 3.75$ to 4.25 range of Ge/Ga compositions yielded multiphase samples exhibiting broad satellites; this, unfortunately, seems to coincide with the ${}^2/_3 \leq q_{rel} \leq 1$ domain of Table 2, over which we find a paucity of structure solutions. Finally at $\delta = 4.50$, we converge on the ScFe$_6$Ga$_6$ end-member.

Having cataloged the geometries of the ErFe$_6$Ge$_{6-\delta}$Ga$_\delta$ phases and the ScFe$_6$Ge$_6$−ScFe$_6$Ga$_6$ intergrowth family as a whole, the question remains: what is driving the structural preferences in this series? The relaxation of the Ge1 honeycombs to accommodate the occupants of the hexagonal cavities recalls the atom size factor that has been evoked for these structures.[20] In the next section, we will examine the role taken by another
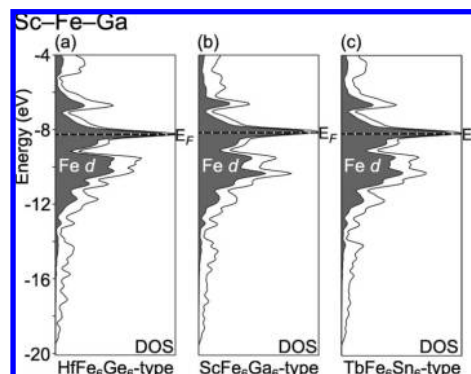
Figure 12. Non-spin-polarized density of states (DOS) curves, calculated at the LDA-DFT level, for ScFe$_6$Ga$_6$ in three structure types. (a) The HfFe$_6$Ge$_6$ structure type. (b) The ScFe$_6$Ga$_6$ structure type. (c) The TbFe$_6$Sn$_6$ structure type. The HfFe$_6$Ge$_6$ and ScFe$_6$Ga$_6$ structure types are the end-members of the intergrowth series discussed in this paper, while the TbFe$_6$Sn$_6$ structure is the simplest example of these intergrowth structures. The Fermi energy (E_F) for each compound is given with a dashed line.

factor, the valence electron concentration, through electronic structure calculations.

4. On the Electronic Structures of ScFe$_6$Ga$_6$−ScFe$_6$Ge$_6$ Intergrowth Phases

4.1. Electron Count as a Factor in the Structural Preferences of This Series. So far in this paper, we have examined in detail the structures of the ScFe$_6$Ge$_6$−ScFe$_6$Ga$_6$ intergrowth series of stuffed CoSn-type structures and their modeling as a 3 + 1D family. We now step beyond structural description toward an understanding of why this amazing variety of stuffing atom occupation patterns occurs. The structural progressions in the REFe$_6$Ge$_{6-\delta}$Ga$_\delta$ (RE = Sc, Lu, Tb, Er) systems provide one alluring clue: across each series the period of the RP function, λ, shrinks monotonically as, starting from the Ge-rich side of the series, Ge atoms are replaced gradually with Ga atoms. Since each Ga atom has one less valence electron than the Ge atom it replaces, this decrease in λ is mirrored by a change in electron count. This suggests the possibility, as put forward by Venturini[33] and discussed above, that there is an electronic origin behind the structural preferences in this series.

To explore this possibility, we performed LDA-DFT calculations on a variety of these structures. A theoretical study of these and related phases is complicated by the emergence of complex magnetic phenomena,[25,26] with often several magnetic states being adopted by a single compound depending on the temperature. While electronic structure calculations have brought insight to these phenomena in the past,[43] our central interest is the factors driving the structural preferences in this series, so we will begin by ignoring these magnetic states, using para-magnetic calculations, in which the up-spin and down-spin wave functions are made equivalent. This will allow us to discern any electronic effect, aside from magnetic ordering, behind the formation of this intergrowth series.

The importance of the Sc-occupation pattern to the electronic structure of these phases can be seen quickly by comparing density of states (DOS) curves for one composition in several structure types in the sequence. In Figure 12, we plot the results for the ScFe$_6$Ga$_6$ ($\delta = 6$) composition for three structure types:

(43) Mazet, T.; Tobola, J.; Malaman, B. *Eur. Phys. J. B* **2003**, *33*, 183–191.

the HfFe$_6$Ge$_6$ ($\lambda = \infty$, $\mathbf{q} = 0$), ScFe$_6$Ga$_6$ ($\lambda = |\mathbf{b}_{ave}|$, $\mathbf{q} = \mathbf{b}^*_{ave}$), and TbFe$_6Sn_6$ ($\lambda = 2|\mathbf{b}_{ave}|$, $\mathbf{q} = {}^1/_2\mathbf{b}^*_{ave}$) types. These correspond, respectively, to the high-λ and low-λ end-members of the series and an intermediate structure.

A first glance at the DOS curves in Figure 12 shows that, while small variations occur, all three curves show a striking similarity in shape. In each, the Fermi Energy (E_F) lies near the tip of a sharp peak in the DOS. This peak is part of a larger dense block of states occurring between ca. -6 and -12 eV. Compact regions of high DOS like this are characteristic of rather localized orbitals, such as the $3d$ orbitals of the Fe. Indeed, the dominance of the Fe d levels here is confirmed by a look at the Fe d contribution to the DOS in this region (shaded); this region corresponds to the Fe d block. For all three structures, the Fe $3d$ block is followed at lower energies by a tail that runs down to ca. -19 eV, consisting mainly of Ga sp states.

From these similarities, we see that the bonding in ScFe$_6$Ga$_6$ is largely unaffected by changes in λ. For each value of λ, the E_F lies at a peak in the DOS, and there is very little advantage for choosing one structure over another at this electron count or, if we follow a rigid band model, at *any* electron count. In fact, calculations on ScFe$_6$Ge$_6$ in these same three structure types (Figure S3 in the Supporting Information) show that the major effect of substituting Ga with Ge is to raise the E_F slightly relative to this DOS peak. This gives an indication for how the extra electrons are accommodated on exchanging Ga with Ge in the ScFe$_6$Ge$_{6-\delta}$Ga$_\delta$ phases: the new electrons are absorbed by the Fe d block. On passing from ScFe$_6$Ga$_6$ to ScFe$_6$Ge$_6$, six new electrons are added to the Fe d per formula unit, amounting to one electron for each Fe atom. These observations hint that the electron count is largely decoupled from the structural preferences within this family.

These indications are further verified by a look at magnetic ordering in these structures. A common element in all these results is the location of the E_F right in the middle of a dense region of Fe $3d$ states. This is a prime opportunity for magnetism. Indeed, repeated observations of complex magnetic effects, such as helimagnetic ordering, have been made in even the simplest of these compounds.[25,26] To model such ordering through LDA-DFT calculations would require large supercells and would require considerable computational time. However, these instances of complex magnetic superstructures are low temperature phenomena, while at high temperatures, the phases exhibit simpler magnetic ordering patterns, such as simple ferro- and antiferromagnetism. Fortunately, the conditions for the simple ordering better approximate those at which these structures initially crystallized. Thus we performed spin-polarized calculations with the LDA-DFT method, restricting ourselves to the primitive unit cell for each structure.

In Figure 13, we show the resulting DOS curves for the ScFe$_6$Ga$_6$ composition in the above-mentioned structure types. As with the non-spin-polarized results above, the curves show a stubborn uniformity from structure to structure. For each one, the sharp DOS peak at the E_F in the non-spin-polarized calculation has given way to a deep hole in the DOS, will a small bump at its center. Such openings in the DOS at the E_F are associated with structural stability, and by this criterion, all three structure types are viable options for ScFe$_6$Ga$_6$.

The similarity of the α-spin DOS curves for all three phases suggests similarities in their magnetic ordering. For all three, an enhancement of the β-spin electrons occurs at approximately the E_F, while the α-spins contribute more just below the E_F. The α-spin electrons then outnumber the β-spin electrons.
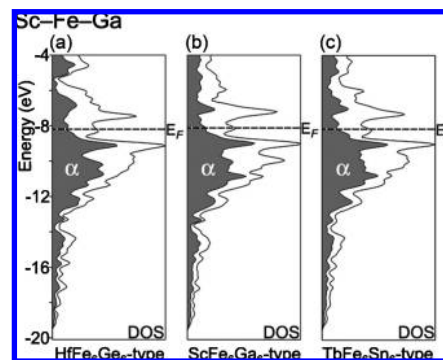
Figure 13. Spin-polarized density of states (DOS) curves, calculated at the LDA-DFT level, for ScFe$_6$Ga$_6$ crystallized in three structure types. (a) The HfFe$_6$Ge$_6$ structure type. (b) The ScFe$_6$Ga$_6$ structure type. (c) The TbFe$_6$Sn$_6$ structure type. The shaded regions show the α-spin contribution to the DOS, the β-spin contribution then being the remainder. E_F: Fermi energy.

Indeed, the resulting ordering pattern is ferromagnetic with 1.56 to 1.62 unpaired electrons on each Fe atom, depending on the structure. Calculations with the ScFe$_6$Ge$_6$ composition showed similar results. This indicates that satisfactory electron configurations are obtainable for all the structures in the ScFe$_6$Ge$_{6-\delta}$Ga$_\delta$ series, for the full range of valence electron counts observed in this series.

From this brief look at the electronic structure of the ScFe$_6$Ga$_6$–ScFe$_6$Ge$_6$ intergrowth structures, it appears that the bonding in these phases is largely unaffected by the presence of the λ modulations. Structurally, this amounts to all relative position patterns of the Sc atoms being permissible in terms of bonding. This recalls the situation with close-packed structures, where the introduction of stacking faults or long-range stacking sequences requires little energy. This confirms the hypothesis put forward in one of the seminal papers on ScFe$_6$Ga$_6$–ScFe$_6$Ge$_6$ intergrowth structure types, in which El Idrissi and co-workers identified five new structure types in REFe$_6$Sn$_6$ compounds, those with RE = Tb, Ho, Er, Dy, and Y.[31] They noted that the structural progression was created with less than a 2% change in the atomic radius of the stuffing atom and inferred that the energetic differences must be small. As further evidence they pointed out that, in several cases, the superstructure adopted depends on the synthesis conditions. The YFe$_6$Sn$_6$ and DyFe$_6$Sn$_6$ compounds were found to crystallize in, respectively, two and three different superstructures, depending on the annealing temperature.

4.2. Modulation of Atomic Charges Mirroring the RP Function. While the structural preferences in this series are weak, we are still faced with definite trends. In the ScFe$_6$(Ge/Ga)$_6$ and ErFe$_6$(Ge/Ga)$_6$ systems, we have already seen the gradual progressions in the q-vector made by changes in the Ge/Ga ratio. Another trend in this family is related to RE atomic sizes. For any given host lattice composition, the larger the RE element, the more frequent the transitions back and forth between RP = 0 and RP = $^1/_2$ regions (shorter λ, larger $\mathbf{q}$). Take the REFe$_6$Sn$_6$ compounds, the first such series to be structurally characterized.[31] In incrementally adjusting the RE ionic radius from 0.81 Å (Sc) to 0.94 Å (Gd), $\mathbf{q}$ monotonically increases, passing (at one annealing temperature) through the values 0, $^1/_4\mathbf{b}^*_{ave}$, $^1/_3\mathbf{b}^*_{ave}$, $^3/_8\mathbf{b}^*_{ave}$, and $^1/_2\mathbf{b}^*_{ave}$.

The density of states (DOS) analysis provided little help in understanding such trends. While it offered clues to the electronic effects stabilizing this family in general, these were
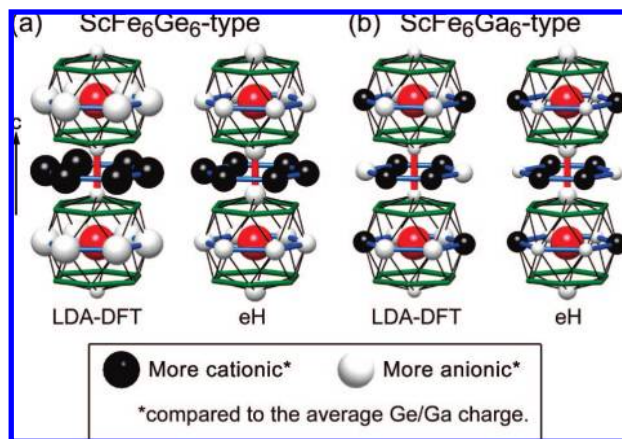
Figure 14. Graphical view of the relative atomic charges for the Ge/Ga sites around the Sc-stuffing atoms in the $ScFe_6Ge_6$ and $ScFe_6Ga_6$ structure types. (a) The $ScFe_6Ge_6$ structure. (b) The $ScFe_6Ga_6$ structure. Relative charges are plotted with spheres, with the sphere volume representing the magnitude of the deviation of that site's charge from the average Ge/Ga charge in the structure. The color gives the sign of the deviation: white for sites that are more anionic than the average, black for sites more cationic. In both (a) and (b) the results from two levels of theory are shown. Left: LDA-DFT charges from a Sc−Fe−Ge calculation, extracted using a Bader Analysis. Right: extended Hückel relative Mulliken populations. Red spheres: Sc positions. Green bars: Fe kagomé net atoms. For calibration of sphere sizes: the largest white spheres and largest black spheres differ in electron population by 0.56 electrons/atom.

found to be invariant with respect to the q-vector. How, then, are we to account for these progressions? As this question is deeply connected to the structures of these phases, let us try turning from the electrons' distribution over the energy axis to their distribution in physical space. We will start with the simplest, most familiar, measure of the electron distribution: the charges of the atoms. In the past, the analysis of atomic charge distributions has brought insight into problems of site preference (i.e., which element goes to which site in a structure) in systems ranging from organic molecules to intermetallic compounds[44−46] and has provided guidance to the description of complex intermetallic structures.[47] In the following, we will see that such an analysis can also be used for teasing out the origins of superstructure ordering.

Upon extracting the atomic charges from our LDA-DFT nonspin-polarized calculations on the $ScFe_6Ge_6$ composition described above, we found, as expected from electron negativity considerations, that the Sc atoms are largely cationic (charge: +1.88e for the $ScFe_6Ge_6$-type), with the Fe being anionic (−0.17e, $ScFe_6Ge_6$-type) and the Ge, on average, being slightly anionic (−0.15e, $ScFe_6Ge_6$-type). Much more intriguing though was the appearance of significant redistributions of the atomic charges upon changes in the placement of the Sc atoms in the structures. While the Sc and Fe charges remained largely constant (with ranges of, respectively, 0.03e and 0.09e over the series of structures calculated), the Ge charges exhibited profound variations that can be used to account for the structural trends in this family of compounds.

We present these Ge charge distributions visually in the left panels of Figure 14a,b for the end-members of this series, the

(44) Longuet-Higgins, H. C.; Rector, C. W.; Platt, J. R. *J. Chem. Phys.* **1950**, *18*, 1174−1181.
(45) Gimarc, B. M. *J. Am. Chem. Soc.* **1983**, *105*, 1979−1984.
(46) Miller, G. J. *Eur. J. Inorg. Chem.* **1998**, 523−536.
(47) Fredrickson, D. C.; Lee, S.; Hoffmann, R. *Angew. Chem., Int. Ed.* **2007**, *46*, 1958−1976.

$ScFe_6Ge_6$- and $ScFe_6Ga_6$-structure types. Here, the hexagonal columns along the c-axis are drawn (cf. Figure 2c). The relative charges are plotted with white and black spheres: Black spheres indicate that the corresponding Ge atoms are more cationic than average, while white spheres mark atoms that are more anionic. The sphere volumes are proportional to the magnitudes of the deviations. The red spheres mark the Sc atom positions.

Differences in both the colors and sizes of the relative charge spheres occur between the $ScFe_6Ge_6$- and $ScFe_6Ga_6$-types, most notably in the blue hexagons derived from the Ge honeycomb layers. In the $ScFe_6Ge_6$ structure (Figure 14a), two very different hexagons occur: those centered by a Sc atom, and those centered by a dumbbell. The Sc-centered hexagons are dotted with plump white spheres; these Ge's are emphatically anionic compared to an average Ge atom in the structure, with an extra 0.26 electrons/atom. The hexagons with the dumbbells are just as emphatically cationic (bearing 0.30 *fewer* electrons/atom than the average). In the $ScFe_6Ga_6$-type, however (Figure 14b), no such clear separation of anionic and cationic character is seen: both the Sc-centered and dumbbell-centered hexagons sport mixtures of relatively anionic and cationic sites, with the overall sizes of the spheres being smaller than those of the $ScFe_6Ge_6$-type. In contrast to these profound differences, the charges on the dumbbell Ge atoms remain largely unchanged between these two structures.

A considerably simpler level of theory, the semiempirical extended Hückel (eH) method, gives quite similar results. In the right panels of Figure 14a,b, we plot the corresponding relative Ge charges, calculated using a Mulliken population analysis. While the methods give somewhat differing results for each structure—the eH method gives sphere sizes that are in general smaller and makes the dumbbell sites too electron rich—there is, however, a remarkable agreement between the methods in the *differences* seen in the charges of the $ScFe_6Ge_6$ or $ScFe_6Ga_6$ structure types. Both methods show virtually no change in the dumbbell sites between the structures. More impressively, both methods agree qualitatively on the differences in colors and relative sizes of the spheres in the hexagons. The eH calculations well reproduce the scrambling of relatively anionic and cationic character on going from the Ge hexagons of the $ScFe_6Ge_6$-type to those of the $ScFe_6Ga_6$-type. The applicability of the orbital-based eH method to this problem shows us that these variations can be understood in terms of chemical bonding concepts, rather than purely physical ones.

The use of the eH method also allows us to perform numerous computational experiments. Being an independent-electron method, the eH calculations can be carried out over a series of electron counts. Such calculations indicate that these charge patterns are largely invariant over the range of electron counts between the compositions $ScFe_6Ge_6$ and $ScFe_6Ga_6$. The relative charge patterns are also stable to numerous variations in the eH parameters. These results are robust enough that we expect the results presented here to be generalizable to the whole structural family.

We can come to a simple rationalization of these relative charge patterns by looking at larger cross sections of the structures. In Figure 15, the honeycomb layers of the $ScFe_6Ge_6$- and $ScFe_6Ga_6$-types are drawn out, with Ge charges relative to the average of the honeycomb charges from the LDA-DFT calculations. Since dumbbell Ge's have a more or less constant charge, from now on we will leave them out of the averaging and take the average honeycomb Ge charge as the reference for the relative charges. The relatively anionic and cationic
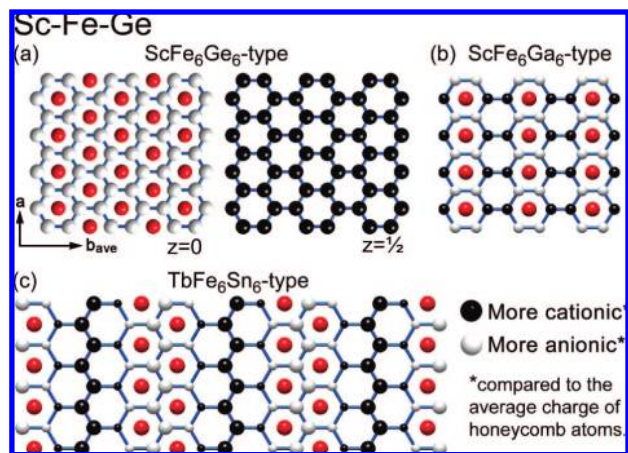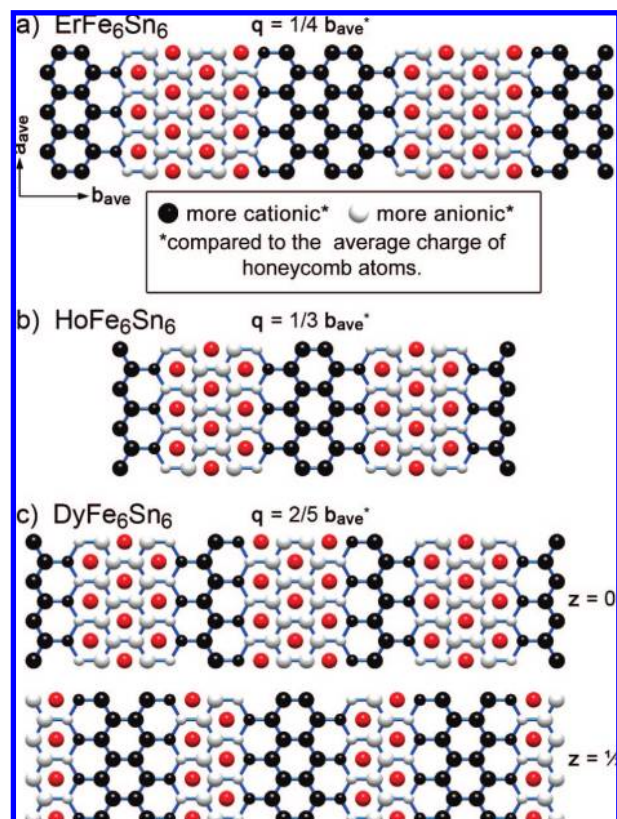
Figure 15. Relative honeycomb charges on the Ge honeycomb sites of the compound $ScFe_6Ge_6$ in the (a) $ScFe_6Ge_6$, (b) $ScFe_6Ga_6$, and (c) $TbFe_6Sn_6$ structure types. The $ScFe_6Ge_6$ structure has two symmetry-distinct honeycomb nets, one with every hexagon occupied by a Sc stuffing atom ($z = 0$), the other without Sc atoms ($z = ^1/_2$). For the other two structures, only one type of honeycomb net is present. See caption to Figure 14 for plotting conventions.

hexagons of the $ScFe_6Ge_6$ structure type become extended here into two symmetry-distinct nets, one consisting purely of white spheres (at height $z = 0$), one completely of black ($z = ^1/_2$). A simple rationalization for this anionic/cationic divide can be gleaned from the placement of the Sc atoms (red spheres). As the RP function is constant throughout the crystal, the placement of Sc atoms is completely in-phase between neighboring hexagonal columns of the structure. This leads to an alteration of honeycombs in which every hexagon is occupied by a Sc atom with Sc-vacant honeycombs. This alternation of layers densely occupied by Sc cations with layers void of such cations, one may reason, prompts a coherent electron transfer between the two types of honeycombs to electrostatically stabilize the Sc cations. Thus the Sc-filled Ge honeycombs appear relatively anionic, with the remaining honeycombs being relatively cationic.

The situation is quite different for the $ScFe_6Ga_6$-type. Neighboring hexagonal channels along the b_{ave}-axis are out-of-phase in their Sc occupations. The result is that all honeycombs in the crystal are symmetry equivalent, each consisting of rows of Sc-centered hexagons separated by rows of empty hexagons. This equivalence means that no net electron transfer can occur between neighboring layers. Instead, the electrons distribute themselves within each layer to maximally stabilize the Sc cations. Two types of Ge atoms can be discerned in the honeycomb, based on their numbers of Sc neighbors (Figure 15b): those with two Sc neighbors and those with one. Those with two Sc neighbors experience a greater cationic pull from the Sc atoms and, thus, appear as relatively anionic compared to the Ge atoms with a single Sc neighbor.

From these observations, the relative charges of the Ge atoms seem directly related to their numbers of Sc neighbors. This tendency is even more clear in the more complex superstructures. Figure 15c illustrates this for the $ScFe_6Ge_6$ composition in the $TbFe_6Sn_6$ structure type. With $n_\lambda = 1$, $n_{sc} = 2$, a single type of honeycomb occurs in which Sc-filled and Sc-vacant bands alternate every two hexagons along b_{ave}. Four symmetry-distinct Ge sites occur in this layer, those with three, two, one, and zero Sc neighbors. These bear charges that are, respectively, strongly anionic, weakly anionic, weakly cationic, and strongly

Figure 16. Relative honeycomb charges for $ScFe_6Ge_6-ScFe_6Ga_6$ intergrowth structures exhibiting large orthorhombic supercells (extended Hückel method, Mulliken population analysis). Relative charges are plotted for the honeycomb layers of the (a) $ErFe_6Sn_6$, (b) $HoFe_6Sn_6$, and (c) $DyFe_6Sn_6$ structure types. See caption to Figure 14 for conventions on plotting relative charges.

cationic (relative to the average honeycomb Ge charge). This creates an almost sinusoidal appearance in the relative charges along the b_{ave}-axis: they switch from highly anionic at the centers of the Sc-filled bands to nearly average at the interface between the Sc-filled and Sc-vacant regions, to relatively cationic at the centers of the Sc-vacant bands. *This wavelike progression occurs with the same repeat length as that for the RP function, creating a modulation in the Ge charges in response to the modulation in Sc atom occupations.*

In Figure 16, we extend these observations to larger superstructures taking advantage of the low computational cost of the eH method. Figure 16a–c show the progression in relative charges for three orthorhombic stuffing patterns of increasing complexity (neglecting the geometrical relaxations within the honeycomb nets in order to isolate the effect of the stuffing patterns; including relaxations leads to only small perturbations in the relative charges). The same transition between comparatively anionic and cationic characters on the Ge sites occurs between regions of Sc occupation and Sc vacancy, respectively. Here, as these regions become larger, the harmonic character seen in the charges of the $TbFe_6Sn_6$-type is less obvious. Instead, as we move away from the (RP = 0)/(RP = $^1/_2$) interfaces, the charges quickly stabilize and become uniform. In fact, the visible deviations from a uniform anionic/cationic division occur only at the Ge sites closest to the interfaces, the only sites where the Ge sites have less than three Sc neighbors. The modulation of the Ge charges in response to the Sc atom RP function closely approximates the discontinuous nature of that function. The phases, then, consist electronically of $ScFe_6Ge_6$-type blocks,

which are separated by sharp antiphase boundaries, with only minor rearrangements of the electron density occurring at these boundaries.

From these atomic charge distributions we can also gain insight into the Ga/Ge ordering in the $ErFe_6Ge_{6-x}Ga_x$ phases, where our refinements from X-ray diffraction data provided little information. The long-tested principle of topological charge stabilization[45] shows the way: the Ge, being more electronegative than Ga, should preferentially segregate to the sites in the structure which show the highest electron populations in a reference calculation, where a single element is placed on all candidate sites. Our model calculations, whether using the $ScFe_6Ge_6$ composition at the LDA-DFT level or a more generic RET_6E_6 composition at the eH level, provide just such reference calculations. In all cases, the electron-rich main group sites cluster around the cationic stuffing atoms, and we predict that the Ge atoms should preferentially occupy these sites. Total energy calculations provide further confirmation of this: non-spin-polarized LDA-DFT calculations on $ScFe_6Ge_5Ga_1$ crystallizing in the $ScFe_6Ge_6$-type indicate that the lowest energy is achieved for placing Ga in the relatively cationic honeycomb layers, with no Sc atoms. The energetic costs for moving the Ga atoms to the dumbbell or Sc-stuffed honeycomb layer are, respectively, 0.13 and 0.15 eV/Ga atom. This order of Ga site preferences (empty honeycomb > dumbbell > Sc-stuffed honeycomb) closely follows the order of electron populations seen in our LDA-DFT calculations on $ScFe_6Ge_6$. These considerations show that Ge/Ga sites in these structures show widely varying affinities for occupation by relatively electronegative or electropositive elements. This, alongside entropy considerations, could account for the tendency for Ge and Ga to combine within the same structure, rather than segregating into separate Ge- and Ga-rich phases.

5. Tension between Electrostatics and Sterics: The Basis for Structural Preferences

5.1. Connecting Modulations of Atomic Positions and Charges to Stability. Our look at the electronic structure of the $ScFe_6Ge_6$–$ScFe_6Ga_6$ intergrowth series in the previous section revealed that the RP function has electronic as well as geometrical consequences: To accommodate the stuffing patterns of the RE atoms, a redistribution occurs in the honeycomb electron populations to maximize the anionic character around these guests. With the strongly cationic character of the RE stuffing atoms, this accumulation of negative charge certainly has a stabilizing effect on the structure. The two end-members of the intergrowth series represent two extrema of this stabilization. In the $ScFe_6Ge_6$ structure, with its uniform RP value throughout the crystal structure, all Sc sites are surrounded by highly anionic honeycomb sites; the electrostatic stabilization cannot get any better than this. The $ScFe_6Ga_6$-type, on the other hand, gives the worst case: the rapid oscillation of RP = 0 and $^1/_2$ regions means that little difference occurs in the anionic characters of the Sc-filled and Sc-vacant hexagons of the honeycomb nets. The other, more complex, superstructures in this series are intermediate between these limiting cases.

All of this points in one direction: toward the stability of the $ScFe_6Ge_6$ structure. The introduction of an (RP = 0)/(RP = $^1/_2$) alternation into the $ScFe_6Ge_6$-type interferes with the structure's ability to stabilize the Sc guest atoms by interrupting its careful concentration of anionic character around them and should then have a destabilizing effect.
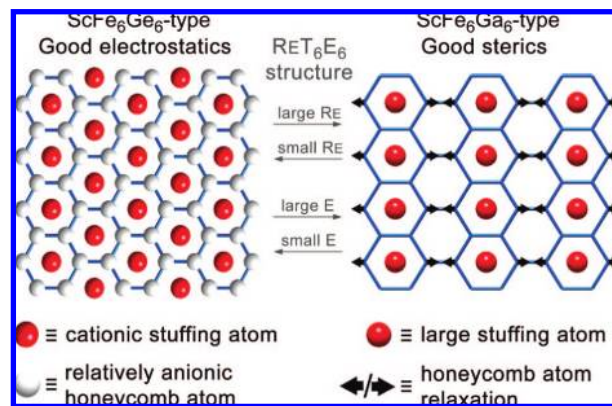
Figure 17. Schematic diagram of the electrostatics/sterics tension model for the structural preferences in the $ScFe_6Ge_6$–$ScFe_6Ga_6$ intergrowth series. Opposing factors stabilize the two end-members. $ScFe_6Ge_6$-type: the arrangement of the cationic guest atoms into tight-packed layers allows them to collectively polarize the host framework and achieve a high degree of Coulombic stability. $ScFe_6Ga_6$-type: the maximal staggering of the guest atoms leads to each filled cavity having several vacant neighbors, enabling relaxations in the host framework structure to accommodate the large size of the stuffing atoms. The intergrowth series arises from various degrees of balance between these two factors. Gray arrows in the middle of the diagram show how the sizes of the stuffing and main group atoms affect this balance.

Why, then, does the $ScFe_6Ge_6$–$ScFe_6Ga_6$ intergrowth series of structures exist? We believe that an essential clue lies in the relaxations made by the host framework in response to the RE occupation patterns. As seen in the $ErFe_6(Ge/Ga)_6$ structure refinements described in section 3, essentially the only atoms to relax are the honeycomb positions (Figure 11c). A positional modulation runs through these atoms affecting most those at the interface between RE-filled and RE-vacant regions. The atoms retreat slightly from the RE atoms into the neighboring RE-vacant hexagons. As we described above, this gives the appearance that the honeycomb atoms are making room to accommodate the large size of the RE atom. If that is indeed the force underlying the honeycomb relaxation, then the (RP = 0)/(RP = $^1/_2$) interface provides stabilization by relieving strain in the distances around the RE stuffing atoms. The stabilization from this relaxation will be maximal for the $ScFe_6Ga_6$ end-member, where the interfaces are most frequent.

Note that this is exactly opposite from the structural preference given by considerations of electrostatics. It seems that opposing forces are at work in this family of phases. Electrostatics clearly favor the $ScFe_6Ge_6$ end-member, while steric repulsion is pushing toward the other end-member, the $ScFe_6Ga_6$-type. Large intergrowths and incommensurate structures are then desperate attempts at compromise. Figure 17 provides a schematic overview of this conflict.

Elemental substitutions can shift the balance in this tension. Consider the $ErFe_6(Ge/Ga)_6$ and $ScFe_6(Ge/Ga)_6$ systems. On going from the Ge-rich to the Ga-rich sides of the composition space, the q-vectors in both systems exhibit a gradual lengthening. The lengthening of the q-vector in reciprocal space corresponds in real space to a shrinking of λ and a shorter distance between neighboring (RP = 0)/(RP = $^1/_2$) interfaces. This progression can be understood from the relative sizes of the Ge and Ga atoms. Upon replacing the smaller Ge with the larger Ga the steric congestion around the Sc/Er atoms becomes exasperated. This added steric stress is relieved by an increased frequency of (RP = 0)/(RP = $^1/_2$) antiphase boundaries. Gray arrows are drawn between the end-members in Figure 17 to

summarize this trend: for a given RET_6E_6 stoichiometry, substitutions on the E site with a larger main group element mean a shrinkage of the $ScFe_6Ge_6$-type blocks of the structure, while substitutions with a smaller main group element lead to an expansion of these blocks. Varying the size of the RE element produces the same effect. As we already described above, using the $REFe_6Sn_6$ series as an example, increasing the RE cationic radius drives the structure toward the $ScFe_6Ga_6$ end of the structural progression.

We should note these trends with elemental substitution hold only when the perturbation from the substitution is relatively small, i.e., where the balance of T–T, T–E, E–E, and other contacts in defining the size of the hexagonal cavity is not seriously upset by the change. Small enough perturbations include the replacement of Ge with Ga, or one RE element with other RE elements. Predicting the structural variations for more serious perturbations proves more difficult. For instance, a disconnect is encountered as we move from the Ge/Ga-based phases, to the Sn-based ones. $ErFe_6Ga_6$ adopts the $ScFe_6Ga_6$-type (reserved for the biggest of E atoms). With the larger size of Sn compared to Ga, we would expect that $ErFe_6Sn_6$ would also crystallize in the $ScFe_6Ga_6$-type. Instead it forms a structure much further on in the continuum toward the electrostatically favored $ScFe_6Ge_6$-type (Figure 4c). Evidently, full replacement of Sn by Ga or vice versa represents too large of a perturbation for a simple size argument to hold. However, the argument still proves useful for small substitutions between Sn and Ga. We will see this in the next section, where we discuss the $ErFe_6Sn_{6-\delta}Ga_\delta$ system.

5.2. The Form of the $ErFe_6Sn_{6-\delta}Ga_\delta$ Phase Diagram. In the $ErFe_6(Ge/Ga)_6$ and $ScFe_6(Ge/Ga)_6$ systems we have looked at so far, the structures for the intermediate Ge/Ga ratios are intermediate between the end-member phases. With our electrostatics vs sterics model in hand, we can now account for the structural chemistry in $RET_6(E/E')_6$ systems with less intuitive structural progressions.[48–50] The $ErFe_6(Sn/Ga)_6$ system provides a particularly pathological example. The Sn-rich end-member, $ErFe_6Sn_6$ (Figure 4c), contains (RP = 0)/(RP = $^1/_2$) antiphase boundaries every four hexagonal cavities along the b_{ave}-direction. In the Ga-rich end-member, $ErFe_6Ga_6$ ($ScFe_6Ga_6$-type, Figure 3b), the frequency of antiphase boundaries increases to the point where they occur at a rate of one per hexagonal cavity along $\mathbf{b_{ave}}$. Normally, we would expect that intermediate Sn/Ga compositions would give rise to intermediate structures, with the frequency of (RP = 0)/(RP = $^1/_2$) interfaces gradually increasing as Sn is replaced with Ga. Instead, the only additional ordered structure type observed in the $ErFe_6Sn_{6-\delta}Ga_\delta$ system is the $ScFe_6Ge_6$-type, in which the (RP = 0)/(RP = $^1/_2$) antiphase boundaries are entirely extinguished!

This $ScFe_6Ge_6$-type domain occurs at compositions near $ErFe_6Sn_4Ga_2$. The prevalence of $ScFe_6Ge_6$-type phases with $RET_6E_4E'_2$ stoichiometries has been explained from the standpoint of atomic size considerations.[48,49] When the E' element is smaller than E, the E/E' ratio of 4/2 allows for just the right balance to build half of the honeycombs entirely from E', with E occupying the remaining honeycomb and the dumbbell sites. The E' honeycombs, with their more open hexagons, then are preferentially occupied by the RE elements. As a result, we obtain the lamellar RE occupation pattern characteristic of the

$ScFe_6Ge_6$ structure type. Examination of the E/E' site ordering, where it has been studied, beautifully confirms this picture.

Our concept of electrostatics/sterics tension provides further insight into the structural preferences in the $ErFe_6Sn_{6-\delta}Ga_\delta$ system and those similar to it. We simply consider how changes in the Sn/Ga composition should effect the balance between these two energetic factors. Starting from the $ErFe_6Sn_6$ end-member, increasing the Ga-content leads to a decrease in the average E atom size. As this relieves the steric strain around the Er atoms, this tips the scale toward electrostatics, and the frequency of antiphase boundaries should decrease. This is consistent with the formation of the $ScFe_6Ge_6$-type phase at the composition $ErFe_6Sn_4Ga_2$. Now let us start from the other end of the Sn/Ga composition. Increasing the Sn-content from the $ErFe_6Ga_6$ end-member raises the average E atom size. As this tips the scale toward sterics, antiphase boundaries should become more prevalent. Since $ErFe_6Ga_6$ already adopts the $ScFe_6Ga_6$-type, with the maximal frequency of antiphase boundaries, substitution with Sn from this end should not lead to any structural changes.

Notice that, on moving from the Sn-rich and Ga-rich ends, we encounter incompatible structural progressions. Going from the Sn-rich end toward intermediate compositions we predict an enhancement of $ScFe_6Ge_6$ character. From the Ga-rich end, however, the $ScFe_6Ga_6$ structure is predicted to hold stable. How will this be resolved as the two progressions meet near the center of the diagram? A two-phase region between the $ScFe_6Ge_6$- and $ScFe_6Ga_6$-type phases would provide one solution. Nature found another way: a domain with no RE/dumbbell ordering (the YCo_6Ge_6 structure type).

With this, the electrostatics/sterics tension model has provided a rationalization for two domains observed for intermediate Sn/Ga compositions in the $ErFe_6Sn_{6-\delta}Ga_\delta$ system: the $ScFe_6Ga_6$-type domain over the range $0.25 < \delta \leq 2.5$ and the YCo_6Ge_6-type one for $2.5 < \delta < 4.0$. Taking together the success of the model seen here for incremental changes in Sn/Ga compositions and its failure for a full exchange of Ga for Sn, we see that the validity of the model for structural predictions is, at this stage, limited to small perturbations in the average atomic sizes.

5.3. Monoclinicity between $q = ^1/_2 b^*_{ave}$ and $q = ^2/_3 b^*_{ave}$. Thus far the electrostatics vs sterics model has, in effect, given us a qualitative partial derivative of the length of the q-vector with respect to the average size of either the RE atoms or E atoms. Can this model also provide insight into the direction of the q-vector, i.e., explain why RET_6E_6 structures sometimes take on monoclinicly modulated phases? This question is particularly relevant to the $ErFe_6Ge_{6-\delta}Ga_\delta$ phases introduced in this paper, where two of the four structures solved are monoclinic (Figure 10). The turning of the q-vector is not unique to the $ErFe_6(Ge/Ga)_6$ system, however. It also occurs in the analogous Sc-, Lu-, and Tb-based series. All of these structures (Table 2) show a departure from the orthorhombic series for monoclinic structures when the q-vector length relative to $\mathbf{b^*_{ave}}$, $q_{rel} = |\mathbf{q}|/|\mathbf{b^*_{ave}}|$, lies in the range $^1/_2 b^*_{ave}$.

In search of an explanation for this trend, we again turn to the relative charges of the honeycomb atoms. In Figure 18, we trace the evolution of these relative charges, obtained from eH calculations, over a series of model structures spanning the $^1/_2 \leq q_{rel} \leq 1$ region of the $ScFe_6Ge_6$–$ScFe_6Ga_6$ intergrowth system. We begin, in Figure 18a, with the structure marking the transition point between the orthorhombic and monoclinic series ($q_x = 0$, $q_y = ^1/_2$). This is the familiar $TbFe_6Sn_6$ structure type, with its double columns of RE-filled hexagons alternating

(48) Ihou-Mouko, H.; Venturini, G. *J. Alloys Compd.* **2005**, *396*, 59–63.
(49) Venturini, G. *J. Alloys Compd.* **2005**, *398*, 42–47.
(50) Venturini, G. *J. Alloys Compd.* **2005**, *400*, 37–42.
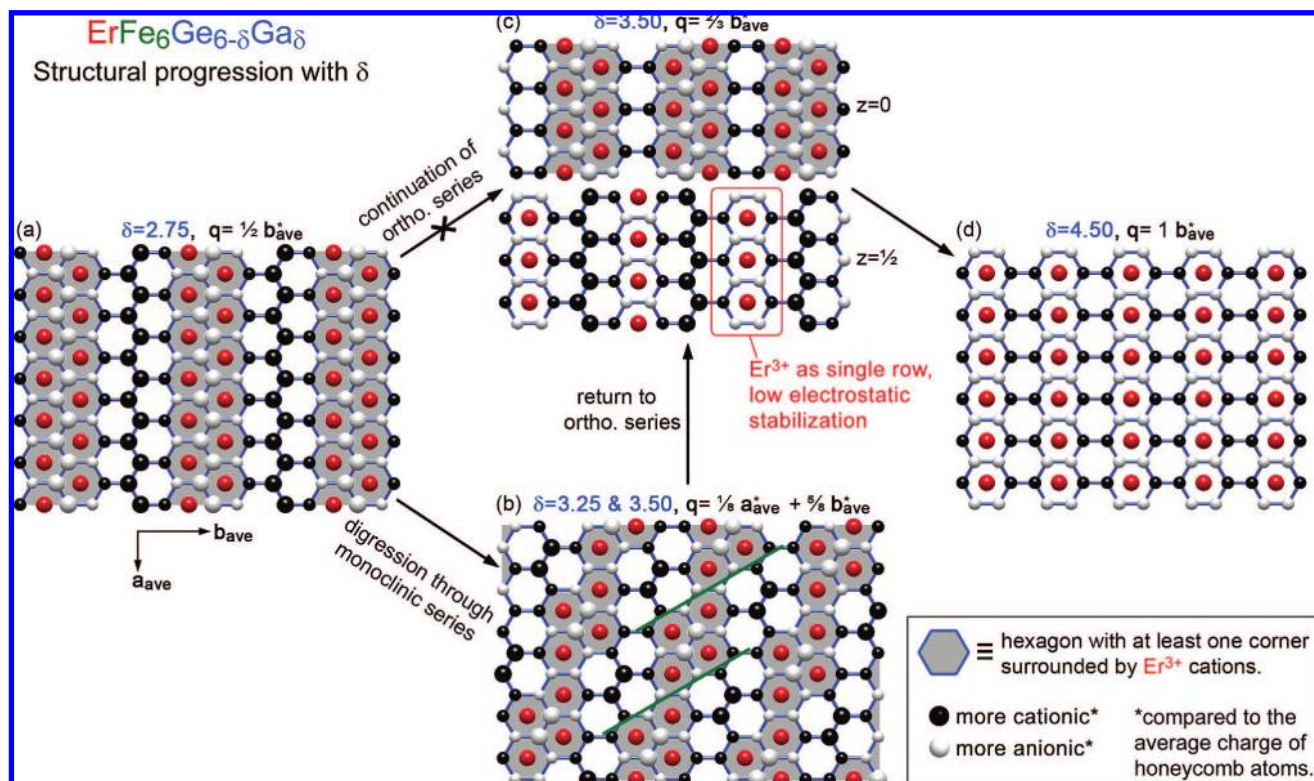
Figure 18. Structural progression observed in the ErFe$_6$Ge$_{6-\delta}$Ga$_\delta$ and other REFe$_6$(Ge/Ga)$_6$ systems monitored with plots of the relative charges of the honeycomb atoms. Relative honeycomb charges derived from Mulliken population analysis of extended Hückel results are shown for model structures exhibiting the q-vectors of (a) the $\delta = 2.75$, TbFe$_6$Sn$_6$-type phase; (b) a commensurate approximant to the monoclinic structures observed in the $\delta = 3.25$ and 3.50 samples; (c) a commensurate approximant to the orthorhombic phase detected in the $\delta = 3.50$ sample; and (d) the $\delta = 4.50$, ScFe$_6$Ga$_6$-type structure. Gray hexagons mark those Er^{3+} cations in contact with at least one highly anionic honeycomb site (honeycomb atoms coordinated on all three sides by Er cations, see text). Note that continuing the orthorhombic series to longer q-vectors than the $\delta = 2.75$ structure necessitates the introduction of single rows of Er cations, as in the bottom of panel (c). These Er cations have no highly anionic honeycomb neighbors. Switching to the monoclinic series (b) allows for an increase in the q-vector length (corresponding to an increased frequency of (RP = 0)/(RP = $^1/_2$) antiphase boundaries), while keeping all Er cations in contact with highly anionic honeycomb neighbors. In (b) green bars indicate slip-planes by which the turning of the q-vector partially dissolves the double rows of Er-filled hexagons seen in the $\delta = 2.75$ structure. See caption to Figure 14 for conventions on the plotting of relative charges.

with double columns of vacant hexagons. As we saw above in Figure 15c, the relative charges in the honeycomb layer show a nearly harmonic distribution: highly anionic and cationic (relative to the average) honeycomb atoms occur at, respectively, the centers of RE-filled and RE-vacant strips of hexagons, and a smooth transition runs between these extremes. This distribution of relative charges is simply related to the numbers of RE cations coordinating each honeycomb site, with those coordinated on all three sides showing the highest anionic character. These highly anionic sites form zigzag chains running along the centers of the RE-filled regions. Every RE cation is coordinated by three such highly anionic neighbors.

This structure forms a critical point in the intergrowth series: the existence of these highly anionic sites in the structure depends on them being coordinated on all sides by RE atoms. This is afforded by the double-hexagon thickness of the RE-filled regions. Reducing the spacing between antiphase boundaries further (increasing q_y) necessitates that some of these double columns of RE atoms are replaced by single columns. The electronic effects of introducing these single columns are shown in Figure 18c, where we plot the relative charges for the $q_x = 0$, $q_y = ^2/_3$ structure. The $z = 0$ and $z = ^1/_2$ layers of this structure are symmetry-distinct, so we draw both of them. In the $z = 0$ layer, only double columns of RE atoms occur; the charge distribution within these columns shows no substantial changes from those of the TbFe$_6$Sn$_6$-type. The $z = ^1/_2$ layer, however, contains RE atoms exclusively in single columns. As

expected, the relative charge patterns around these RE atoms match closely those of the ScFe$_6$Ga$_6$ end-member (Figure 18d). No highly anionic sites coordinate these $z = ^1/_2$ RE atoms.

Continuing the orthorhombic series to $q_y > ^1/_2$ thus represents a sudden change in the electrostatic stabilization of the structures: from a structure where all RE atoms have three highly anionic honeycomb neighbors, we go to structures where an increasing fraction of the RE atoms have no such neighbors. At $q_y = ^2/_3$, this fraction is as high as one-third.

Coupling the increase in length of the q-vector with a monoclinic turning allows for a more gradual reduction of the electrostatic stabilization of the RE stuffing atoms. As explained in section 3, the turning of the q-vector in the $\mathbf{a}^*_{\text{ave}}-\mathbf{b}^*_{\text{ave}}$ plane has the effect of introducing slip-planes into the double columns of RE atoms in the TbFe$_6$Sn$_6$ structure type. Figure 18b demonstrates how these slip-planes perturb the relative charges of the honeycomb layer, taking as an example the commensurate approximate ($q_x = ^1/_8$, $q_y = ^5/_8$) to the monoclinic phases observed in the ErFe$_6$Ge$_{6-\delta}$Ga$_\delta$, $\delta = 3.25$ and 3.50 samples. Two slip-planes in this structure are highlighted with green bars. At each slip, several honeycomb atoms that were originally triply RE-coordinated in the TbFe$_6$Sn$_6$-type become only doubly coordinated. However, the spacing of the slips at every two hexagons along $\mathbf{a}_{\text{ave}}$ is sparse enough that substantial anionic character can still build up between the slips. The result is that the infinite zigzag chains of highly anionic atoms at $q_x = 0$, $q_y = ^1/_2$ have become truncated to pairs of atoms. While this

structural change seems rather drastic, every RE atom in the structure is still in contact with at least one highly anionic site.

In essence, the turning of the q-vector as q_{rel} exceeds $^1/_2$ stems from a change in the way the structures mediate the balance in the electrostatics−sterics tension. From $q_{rel} = 0$ to $^1/_2$, electrostatics gradually relinquished structural control to sterics through the process of thinning down the $ScFe_6Ge_6$-type blocks. Rather than continuing this beyond $q_{rel} = ^1/_2$, obeisance is paid to sterics through the introduction of slips into the $TbFe_6Sn_6$-type double columns. Increasing the length of the q-vector over this range corresponds to a decrease in the spacing between these slips. This effect can be observed in the $ErFe_6Ge_{6-\delta}Ga_\delta$ system (Figure 10). The $\delta = 2.75$ phase forms the $q_{rel} = ^1/_2$ phase. Upon increasing δ, the q-vector begins lengthening and turning. At $\delta = 3.00$, with slips occurring at a predominant spacing of every three steps along the a_{ave}-direction. At $\delta = 3.25$, the lengthening and turning are more pronounced: the slips now occur every two steps along $\mathbf{a_{ave}}$.

A new critical point in the $ScFe_6Ge_6-ScFe_6Ga_6$ series is reached at the $q_x = ^1/_8$, $q_y = ^5/_8$ structure (Figure 18b). Increasing the frequency of slips further forces at least some RE atoms to be in contact with slip-planes on both sides along the a_{ave}-axis. These atoms would have local environments resembling those of the $ScFe_6Ga_6$ structure type, without contacts to any highly anionic sites. At this point, the advantages of the monoclinic series relative to the orthorhombic one are lost, and the orthorhombic series can resume. The q_{rel} value 0.661 for this structure matches well with the shift back to the orthorhombic series seen in Table 2. The two-phase region represented by the $ErFe_6Ge_{6-\delta}Ga_\delta$, $\delta = 3.50$ sample, described in section S2.4 of the Supporting Information, marks this transition back to the orthorhombic series.

6. Conclusions

A pervasive structural theme links the superstructures formed in the stuffed CoSn-type phases. With only a couple exceptions, the structures are built from domains of the $ScFe_6Ge_6$ structure type, in which the stuffing atoms in the CoSn-type framework seem to attract each other, forming lamellar arrangements. These domains are terminated by antiphase boundaries which bear the structural features, locally, of the $ScFe_6Ga_6$ structure type. The full possibilities inherent in this scheme constitute the $ScFe_6Ge_6-ScFe_6Ga_6$ intergrowth series, which describes structures formed in more than 200 ternary and pseudoternary systems. In this paper, we have developed—through a program of superspace analysis, synthesis, structure refinement, and electronic structure calculations—a unified description of this structural family and an explanation for the factors driving the structural preferences.

Starting from the $ScFe_6Ge_6$ and $ScFe_6Ga_6$ end-members, we developed a superspace model for the intergrowth series. In this model, a single 3 + 1D unit cell forms the basis for the whole family. The variation in widths and orientations of the $ScFe_6Ge_6$-type blocks across the family are handled by simply changing the cell parameters of this unit cell (and stepping along supergroup−subgroup relations between the orthorhombic and monoclinic series). While this method serves as a convenient way to catalog the commensurate members of this family, its usefulness is much more evident in the incommensurate phases of this family, where the lack of 3D periodicity impedes a comprehensive structural description in physical space.

The superspace model also provides a basis for the structural refinement of the incommensurate members of the series. We

demonstrated this with the structure solutions of four new phases in the $ErFe_6Ge_{6-\delta}Ga_\delta$ system from powder X-ray diffraction data. These refinements vividly showed that the structural relaxation around the stuffing atoms in these phases is minor. Aside from the dumbbell formation along the c-axes of these phases, only one significant positional modulation mode was detected. This modulation affects the honeycomb networks, the hexagons of which serve as belts around the stuffing atoms and dumbbells, creating a slight contraction around the dumbbells and expansion around the stuffing atoms. This creates the impression that the stuffing atoms are just a little too big for the hexagonal cavity to accommodate without stress.

The minuteness of these distortions at the geometrical level is reflected in the results of electronic structure calculations. The features of the density of states (DOS) curves appear unperturbed as we move from one superstructure ordering pattern to the next. The ability of a phase to form an opening in the DOS at the Fermi energy through magnetic ordering remains intact after variations in structure, electron count, and composition. The rigid form of the DOS in this family allows for more minor factors to play decisive roles in the structural trends. The two key players uncovered here are the steric strain around the stuffing atoms (revealed in the structure refinements) and an induced polarization of the atomic charges created by the presence of the highly cationic stuffing atoms.

These results can be woven into a concise scheme for the cooperativity between the stuffing of neighboring hexagonal cavities in the CoSn-type. When a single hexagonal cavity of this structure is stuffed with an electropositive RE atom, the stuffing atom sends mixed messages to the neighboring hexagonal cavities. First, the stuffing atom's size distorts the walls of the cavity, pushing the walls into the spaces of the neighboring cavities. This, of course, tends to make the neighboring interstitial spaces unattractive to other stuffing atoms. This is the dominant effect along the c-axis, along which the RE/dumbbell alternation occurs. In addition to this steric signal, the RE sends an attractive signal: its cationic character polarizes the CoSn-type framework, creating a high electron density in the cation's immediate surroundings. This concentration of negative charge serves as a beacon to other stuffing atoms. The steric repulsion message alone calls for the formation of the $ScFe_6Ga_6$ end-member of the intergrowth series, while the electrostatic signal by itself directs crystallization in the $ScFe_6Ge_6$ end-member. Varying the relative strengths of the two signals creates the full intergrowth series.

This provides an explanation for the major structural trends within the $REFe_6(Ge/Ga)_6$ systems and other systems where elemental substitution creates minor perturbations to the hexagonal cavity dimensions, including the formation of a monoclinic series as the $ScFe_6Ge_6$-type blocks become exceedingly narrow. So far, these considerations have been made in an entirely qualitative manner. There, however, is the prospect of developing these ideas in a quantitative way, moving toward predictions of the structure type a phase will adopt from its composition.

Tension between two driving forces directing the structure in opposite directions: what could be a simpler origin of complex superstructure ordering and even incommensurability? Perhaps a similar dynamic underlies other systems exhibiting these phenomena. One particularly intriguing place to look might be in the ordering of interstitial defects in alloys.

7. Technical Procedures

Synthesis. The samples $ErFe_6Ge_{6-\delta}Ga_\delta$ were prepared from a mixture of the ternary alloys $ErFe_6Ge_6$ and $ErFe_6Ga_6$ previously synthesized from the elements in an induction furnace. This route of synthesis avoids the manipulation of small quantities of gallium which is problematic due to its low melting point. The stoichiometric amounts of the ternary compounds were finely ground to ensure homogeneity and compacted into pellets using a steel die. The pellet was then put into an alumina tube and sealed in a silica tube under argon (100 mmHg). The samples were then annealed for 1 week, at 950 °C for $\delta = 2.75$ and 4.5 and at 900 °C for $\delta = 3.0$, 3.25, and 3.5.

Data Collection on Powder Samples. The compounds were analyzed by X-ray diffraction using a Guinier camera with Co Kα_1 radiation. The patterns were scanned with an LS-20 Line Scanner, and the measured Bragg angles and corresponding interreticular distances were used to check the crystallographic properties of the various samples. Estimation of the q-vector components was done using the graphical method in the reciprocal lattice. These components were then refined with a least-squares procedure together with the basic cell parameters. The diffraction intensities were also recorded on an XPert Pro diffractometer using Cu Kα radiation for use in Rietveld refinements.

Rietveld Refinements. Rietveld refinements were carried out using the JANA2000 package.[42] For each sample, the powder profiles were modeled with a single Pseudo-Voigt peak-shape function, and the background correction was made with a 10-term Legendre polynomial. The atomic coordinates of the impurity phases were held fixed, but their unit cell parameters were allowed to vary while respecting the restrictions of their space group symmetry. The Pseudo-Voigt peak-shape parameters for the impurity phases were set equal to those of the major phase. Further details on the Rietveld refinements can be found in section 3.

Electronic Structure Calculations. Electronic structure calculations on the $HfFe_6Ge_6$, $ScFe_6Ga_6$, and $TbFe_6Sn_6$ structure types were calculated at the LDA-DFT level using the VASP package.[51–54] The calculations were done with the ultrasoft pseudopotentials provided with the package in high-precision mode, corresponding to an energy cutoff of 297.0 eV for both the Sc−Fe−Ge and Sc−Fe−Ga systems. Atomic charges were obtained for the Sc−Fe−Ge system with a Bader charge analysis,[55] using the code of Arnaldsson, Tang, and Henkelman.[56,57] Quantum mechanical calculations were also carried out at the semiempirical level using the extended Hückel (eH) method with the YAeHMOP program.[58] The eH parameters were based on those of Sc, Fe, and Ga optimized by Cerdá and Soria to more accurate tight-binding calculations.[59] Further details on the calculations at both levels of theory can be found in section S4 of the Supporting Information.

Supporting Information Available: Derivation of the 3 + 1D space group symmetry of the stuffed CoSn-type phases; further details on the Rietveld refinements of and electronic structure calculations on $ErFe_6(Ge/Ge)_6$ structures; and a crystallographic information file (CIF) containing the structure refinement data for the four $ErFe_6(Ge/Ga)_6$ phases refined in this work and the original powder data. This material is available free of charge via the Internet at http://pubs.acs.org.

JA077380+

(51) Kresse, G.; Hafner, J. *Phys. Rev. B* **1993**, *47*, 558–561.
(52) Kresse, G.; Hafner, J. *Phys. Rev. B* **1994**, *49*, 14251–14269.
(53) Kresse, G.; Furthmüller, J. *Comput. Mater. Sci.* **1995**, *6*, 15–50.
(54) Kresse, G.; Furthmüller, J. *Phys. Rev. B* **1996**, *54*, 11169–11186.
(55) Bader, R. F. W. *Chem. Rev.* **1991**, *91*, 893–928.
(56) Henkelman, G.; Arnaldsson, A.; Jónsson, H. *Comput. Mater. Sci.* **2006**, *36*, 354–360.
(57) Sanville, E.; Kenny, S. D.; Smith, R.; Henkelman, G. *J. Comput. Chem.* **2007**, *28*, 899–908.
(58) Landrum, G. A. *YAeHMOP: Yet Another extended Hückel Molecular Orbital Package, Version 3.0b.*; YAeHMOP is freely available on the WWW at URL: http://sourceforge.net/projects/yaehmop/.
(59) Cerdá, J.; Soria, F. *Phys. Rev. B* **2000**, *61*, 7965–7971.